MODELING THE SPATIAL DISTRIBUTION OF COMPLEX FRACTURE SYSTEMS AND ITS IMPACT ON UNCONVENTIONAL RESERVOIR PERFORMANCE WITH DISCRETE FRACTURE NETWORKS

A Thesis

by

JINGJING ZHANG

Submitted to the Office of Graduate and Professional Studies of
Texas A&M University
in partial fulfillment of the requirements for the degree of

MASTER OF SCIENCE

Chair of Committee,	David Schechter
Committee Members,	Maria A. Barrufet
	Berna Hascakir
Head of Department,	Jeff Spath

May 2021

Major Subject: Petroleum Engineering

ABSTRACT

The presence of natural fractures is one of the major factors for hydrocarbon production and a proper method to incorporate their characterization into the reservoir model are of critical importance for shale reservoirs. This study utilizes discrete fracture network (DFN) modeling as the powerful tool to investigate the spatial distribution of subsurface fracture systems and its dynamic impact on shale reservoirs for optimal field development.

We first present a summary of important field data acquisition programs and an overview of natural fracture characteristics commonly observed in the field, and then propose a workflow to develop DFNs by in-house software. Three types of DFN models are established to meet different research demands, including an outcrop-based model, a conceptual model and a stochastic model.

From each of these models, the outcrop model extracts natural fractures (NF) from the outcrop map to directly represent the distribution of fracture length, fracture spacing and fracture strike for modeling, as it is widely believed that fracture patterns exposed on the surface provide analogous information for subsurface fracture networks. The second synthetic model consists of a horizontal well and multiple hydraulic fractures (HF). The model is developed to explore the possibility of more advanced and complex completion designs rather than traditional uniform stimulation treatment. The third stochastic model adopts the fractal theory that believes the correlation between fracture characteristics and sampling domain size is consistent over different fractal dimensions, to populate fracture

distribution over the modeling domain. The Hydraulic Fracturing Test Site (HFTS) in Midland Basin is demonstrated as the field case, along with a detailed history matching process.

Once the DFN model is developed, our software will export the fracture model and the calculated connection list to a commercial simulator to perform numerical reservoir simulation, enabling further research of the sensitivity of NF characteristics, reservoir production evaluation and stimulation treatment optimization.

DEDICATION

To my parents, Dengbo Zhang and Kui Jia, for your unconditional love and support.

To my friends, for accompanying me and sharing my ups and downs.

To myself, for the courage and enthusiasm towards life.

ACKNOWLEDGEMENTS

I would like to express the greatest gratitude to my committee chair, Dr. David Schechter, for his consistent support, patience and encouragement during this study. His words ‘calm down, work hard and hang tough’ guides me through my graduate research life.

I would like to thank my committee members, Dr. Maria A. Barrufet and Berna Hascakir, for their kind attention and generous assistance to my research progress.

Thanks also go to my lovely and respectful colleagues in the research group, Wayan Rakananda Saputra, Geng Niu and Fan Zhang for discussing and sharing their knowledge with me. Thank other research group members, the department faculty and staff for making my time at Texas A&M University a great experience.

CONTRIBUTORS AND FUNDING SOURCES

Contributors

This work was supervised by a thesis committee consisting of Professor David Schechter and Professor Berna Hascakir of the Department of Petroleum Engineering and Professor Maria A. Barrufet of the Department of Chemical Engineering.

The in-house software coded with MATLAB is partly developed based on the works of fellow researchers including Tae Hyung Kim, Jianlei Sun and Geng Niu.

All other work presented in this thesis was completed by the student independently.

Funding Sources

Graduate study was supported by the Crisman and Berg-Hughes Integrated Research Program at Texas A&M University.

This work was also made possible in part by the research fellowship provided by the Harold Vance Department of Petroleum Engineering at Texas A&M University.

NOMENCLATURE

DFN	Discrete Fracture Network
NF	Natural Fracture
HF	Hydraulic Fracture
SRV	Stimulated Reservoir Volume
HFTS	the Hydraulic Fracturing Test Site
UCW	Upper Wolfcamp Well
MCW	Middle Wolfcamp Well
SCW	Slant Well
DFIT	Diagnostic Formation Injection Tests
EIA	United States Energy Information Administration
EOR	Enhanced Oil Recovery
PDF	Probability Distribution Frequency
CDF	Cumulative Distribution Function
DP	Dual-porosity
BHP	Bottomhole Flowing Pressure
PEBI	Perpendicular Bisector
FMI	Formation Micro Imager
LGR	Local Grid Refinement

TABLE OF CONTENTS

Page

LIST OF FIGURES

Page

LIST OF TABLES

Page

CHAPTER I

INTRODUCTION AND LITERATURE REVIEW

Research Background

Unconventional reservoirs have become the common target of hydrocarbon extraction over the decades. The US Energy Information Administration (EIA 2020) reports that tight oil accounts for about 70% of the cumulative oil production of the US in 2020 and this number will continue to rise. The presence of underground natural fractures is one of the major factors for hydrocarbon production from shale reservoirs and its importance was realized for the first time due to unexpected production behaviors in many early fields (Narr et al. 2006). Production peaks at the beginning of the primary depletion process, shortly thereafter, a steady flow with low decline rates continues for a long time. The substantial contrast between the fracture permeability and the matrix permeability in poorly permeable shale formation (usually 1e-6 mD to 1e-4 mD) accounts for this phenomenon and makes the diagnosis of natural fractures more important than it is in conventional plays. The hydrocarbon migration and reservoir productivity of unconventional reservoirs greatly depends on the connectivity and conductivity of the fracture network as well as the transfer between the fracture and reservoir matrix. In this regard, the knowledge about the spatial distribution of natural fractures is very important.

Horizontal wells with multi-stage stimulation treatment have been widely adopted as a solution to generally unfavorable recovery rates of shale reservoirs. Large-scale field data acquisition projects have been carried out in major unconventional plays in the United

States to characterize the reservoir and the fracture systems therein. **Table 1** lists a few well-known projects that focus on direct fracture sampling and their operators, lithology, hydrocarbon types, extracted cores, interpreted hydraulic and natural fracture information based on cores, along with other data obtained from fields. The reason why we want to construct such a table is to give an idea of what kind of field information we can obtain to characterize the fractured reservoir.

Table 1 Summary of Important Field Data Acquisition Programs.

Shale Sites	Lithology	Hydrocar-bon Type	Matrix Permeability,uD	Cores	NF	HF	Other Data	Operators
MWX in Piceance Basin, CO	sandstone & siltstone	tight gas	0.1 - 2	over 4200 ft vertical core with diameter of 4 in	among 450 fractures of different types, subvertical fractures that strike W-N are most abundant	N/A	basic geophysics and well test data	DOE, 1981
SHCT in Piceance Basin, CO				266 ft slant core with diameter of 4 in and 115 ft horizontal core with diameter of 2.625 in	65 similar fractures as MWX's, width ranging from 0.01 - 0.15 in	HFs strike in the same direction as NFs	outcrops, logs, buildup and production tests	DOE, 1991
B-sand of Multi-Site Project in Piceance Basin, CO				slant core, 126 ft away from the fractured MWX-2 well	N/A	11 far-field vertical fractures that are clustered and parallel to each other	standard and borehole image logs, GR tracer identification, pressure transient data, proppant recovery data,fracutre conductivity test, production logging surveys, microseismicity	GRI and DOE, 1996
Two-well COOP program in Antrim Shale, MI	shale	gas and coalbed methane	2.00E-05	2 slant cores with one 75 ft away from fractured well and one 125 ft away, 2 NFs and a few HF groups captured	2 sets of subvertical NFs striking N-E and N-W respectively, intensive	complex HF growth, probable subvertical HFs striking N-E in the same direction as primary NFs and potential horizontal HFs	standard and borehole image logs, injection/falloff tests, GR tracer identification, pressure transient data, PVT data	GRI, 1992
1U and 5U zone of Upper Spraberry in Midland Basin, TX	sandstone & siltstone	oil	<1000	19 horizontal cores with total length up to 395 ft and diameter of 2.625 in	102 vertical fractures comprised of 2 systems: one evenly spaced group striking N43°E in the upper layer and another 2 sets striking ~N33°E and ~N70°E respectively	low injection rate makes HFs obey the primary NFs' trend while high injection rate leads to disperse HFs	standard and borehole image logs, well tests and well interference data	Joint project, funded by DOE, 1996
Eagle Ford in DeWitt County, TX	shale	oil	0.01-1.2	3 horizontal cores with total length up to 680 ft and diameter of 3 in	rare	striking N60 °E, subvertical, non-uniformly spaced doublets or triplets	standard and borehole image logs, microseismicity, DTS/DAS, radioctive proppant tracer, pressure monitoring data	ConocoPhi l-lips, 2014
HFTS in Midland Basin, TX	shale	oil	0.2-0.8	6 slant cores with diameter of 4 in and total length of 600 ft	2 sets of calcite-sealed NFs, striking ~N76°E and ~N46°W respectively, subvertical. NFs in the Upper Wolfcamp are 5 times more extensive than those of Middle Wolfcamp layer	subvertical, striking perpendicular to the minimum horizontal in-situ stress	outcrop, standard and borehole image logs, microseismic and seismic surveys, micro DFIT, pressure monitoring data, fluid and proppant tracers	Joint industry, 2015

Notes: 1. MWX = the Multiwell Experiment
2. SHCT = Slant-Hole Completion Test
3. HFTS = the Hydraulic Fracture Test Site
4. DOE = the Department of Energy
5. GRI = the Gas Research Institute
6. GR tracer = gamma ray tracer
7. DTS = Distributed Acoustic Sensing; DAS = Distributed Temperature Sensing
8. DFIT = Diagnostic Formation Injection Tests

Since 1981, the Department of Energy (DOE) has launched serial projects in the Piceance basin, Colorado. The first Multiwell Experiment Site (MWX) was designed to

characterize the tight gas sand and assess its producing technology. Three vertical wells were drilled and plenty of vertical cores were extracted to identify natural fractures. After the completion of MWX, a fourth deviated well of Slant-Hole Completion Test (SHCT), as part of the second project, was drilled for the purpose of testing deviated and horizontal drilling's application in the same shale play. While this new strategy of horizontal well development was proved to be successful in producing gas resources relative to conventional vertical wells, the comparison between the vertical cores obtained by MWX and low-angle (slant and horizontal) cores obtained by SHCT from the same site was also very inspiring. On the one hand, low-angle cores were found to be able to capture more fractures as most of them were at high angle to the bedding and provide more information about fracture spacing, frequency, and porosity. On the other hand, these low-angle cores became one of earliest direct observations of complex post-frac systems that consist of non-activated natural fractures, activated natural fractures and hydraulic fractures. Hydraulic fractures induced by adjacent stimulated wells propagate in the form of swarms instead of simple bi-wing fracture planes as previously anticipated (Finley and Lorenz 1989; Lorenz and Hill 1994). Later on, as more and more other field samples were collected, people began to realize the degree of hydraulic fracture branching/bifurcating/clustering/swarming had been greatly underestimated.

In 1996, another follow-up slant well as part of the Multi-Site Hydraulic Fracture Diagnostics Project was drilled 126 ft away from the fractured MWX-2 well with emphasis on testing microseismic technique. More diagnostic field data such as radioactive tracer and proppant recovery were gained as exploration techniques advanced

over years. Eleven far-field vertical hydraulic fractures that were clustered and parallel to each other were observed in the core and verified through multiple information sources (Branagan et al. 1996).

In 1992, in order to optimize the completion and stimulation technology for Antrim Shale in the Michigan Basin, the Gas Research Institute (GRI) launched a two-well COOP program. Both NFs and HFs were captured by slant cores but they were two few to characterize the whole fracture system. Combined with a series of tests including mechanical test, logs and production data analysis, two sets of sub-vertical NFs were identified in the direction of N-E and N-W, respectively. It was inferred that HF system constituted probable sub-vertical HFs striking N-E and potential horizontal HFs (Hopkins et al. 1995).

In 1996, a joint project funded by DOE was designed to test the feasibility of CO_2 flooding in Spraberry formation, one of the largest reserves worldwide with giant oil in place but low recovery. Two distinct NF systems were found in horizontal cores: one evenly spaced group striking N43°E in the upper layer and the other pair of less mineralized sets striking ~N33°E and ~N70°E in a lower pay zone. The existence of natural fractures results in severe permeability anisotropy and complexity in reservoir characterization (Montgomery et al. 2000; Lorenz et al. 2002).

In recent years, the observation of subsurface fracture populations has benefited from the development of high-tech exploitation techniques. In 2014, ConocoPhillips conducts an experiment in the Eagle Ford formation in DeWitt County, Texas. A large number of HF doublets or triplets and very limited natural fractures are found in horizontal

cores whose total length is up to 680 ft. One remarkable finding is that the number of hydraulic fractures near the wellbore greatly exceeds the number of clusters and decreases as it moves vertically and horizontally away from the wellbore, verifying the complexity of hydraulic fracture growth pattern. In addition, microseismic data can provide a reliable estimate for the extension of stimulated reservoir volume (SRV), but microseismic event density barely matches the directly sampled fracture density (Raterman et al. 2017).

In 2015, the Hydraulic Fracturing Test Site (HFTS) in Midland Basin, west Texas, is launched by the joint industry. This $25 million program applies miscellaneous state-of-the-art measurements in both Upper and Middle Wolfcamp formations. This project involves six Upper Wolfcamp wells (UWC), five Middle Wolfcamp wells (MWC) and one slant well (6TW or SWC) with 82-degree inclination. Over 400 stages of fracturing treatment were conducted on these 11 horizontal wells. Unprecedentedly, over 700 fractures including HFs, non-activated NFs and activated NFs are captured and clearly identified from the slant cores. Multiple information sources such as microseismicity, formation micro imager (FMI) logs and well interference data mutually verify the effectiveness of each other, promising the most precise description of the fracture system. It is discovered that the simulated fracture extension is much smaller than the propped fracture size with the latter being of major interest to reservoir engineers (Courtier et al. 2017; Campbell et al. 2018; Gale et al. 2018).

Introduction to Fractured Reservoir Simulation

To make full use of in-situ evidence of the fracture system described above, an appropriate modeling approach is very important. Numerical methods of fluid flow simulation in fractured reservoirs can be divided into four categories: continuum, discrete, equivalent continuum and hybrid models. The continuum approach simplifies the porous media as uniformly distributed and well-connected fracture channels and matrix blocks, amongst which the simplest dual-porosity (DP) model, also known as sugar-cube model, was initially introduced by Warren and Root in 1963 to simulate single-phase hydrocarbon flow in naturally fractured reservoirs. Every block of DP model is divided into matrix part as the primary porosity that provides hydrocarbon storage and fracture part as the secondary porosity that contributes to the fluid flow. The fluid transfer only occurs between the fracture and matrix, and is assumed to reach the pseudo-steady state.

On the basis of DP, many other models were proposed. For example, DP was extended to dual-porosity dual-permeability (DPDK) model by Kazemi et al. (1976) to allow additional matrix-to-matrix fluid transfer and multiphase flow. Matrix permeability is no longer necessarily low. Besides, multiple interacting continua (MINC, Pruess and Narasimhan 1985) model and SUBDOMAIN model (Beckner et al. 1991; Fung 1991) were brought up to account for transient effect and gravity segregation near fracture, in which one matrix block was divided into nested rings and several layers, respectively. The schematic diagrams of flux transfer paths in those models are shown as **Fig.1**. A more recent multiple-porosity (MP) model was used to model a system composed of different pore types (Yan et al. 2016).

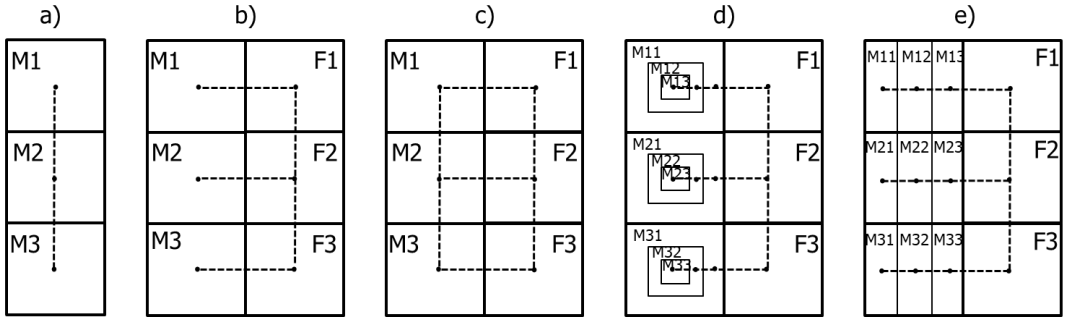

Figure 1 Schematic diagram of a 1-D column of grid blocks, modeled as a) single-porosity model for unfractured reservoir; b) DP model; c) DPDK model; d) MINC model; 3) SUBDOMAIN model. Modified from Doughty (1999).

The advantages of the discrete fracture model (Karimi-Fard and Firoozabadi 2003; Monteagudo and Firoozabadi 2004), the second computational method, over continuum models are that realistic fracture network geometries and their petrophysical properties are explicitly expressed rather than being idealized or averaged in modeling. This is extremely important for flow characterization in unconventional reservoirs of high heterogeneity. The accurate expression of complex fracture features such as clustering or low-angle intersections in the DFN makes it a mesh-dependent computational approach. More specifically, irregular matrix grids such as triangular grids, unstructured PEBI (perpendicular bisector) or Voronoi grids need to be generated to conform to the geometry of fractures precisely. Flexible unstructured grids are also capable of reducing grid orientation effect and total number of grids (Heinemann et al. 1991; Cipolla et al. 2011; Fung et al. 2013).

The third approach, equivalent Continuum Model (ECM), is a mesh-free method that implicitly incorporates fracture properties into background matrix medium. For example, the widely accepted embedded discrete fracture model (EDFM) proposed by Lee

et al. was one kind of ECM (Lee et al. 2001; Li and Lee 2008; Moinfar et al. 2014). Each fracture plan is embedded within structured matrix cells and is discretized by cell boundaries. The fracture-to-fracture and fracture-to-matrix flow inside of the polygon fracture domain is computed as additional transmissibility and will be added to the matrix grid. EDFM shows great efficiency and simplicity, however, it is unable to capture the transient flow behavior in matrix.

To compensate the shortage of each numerical method, many hybrid models such as SUBDOMAIN + DPDK (Rubin 2007), EDFM + MINC model, continuum + DFN model (Jiang and Younis 2016), EDFM + DP model (Xu et al. 2019) and so forth were also brought up.

Among all the numerical fracture modeling methods, only DFN is the most precise type without any degree of averaging or approximation and will be chosen as the basic tool for flow simulation in this study. Multiple ways of discrete fracture models development will be illustrated in the next chapter. (Darcel et al. 2003; Lei et al. 2017; Niu 2019).

Introduction to Statistical Characteristics of Natural Fractures

Naturally existing discontinuities can be mechanically divided into three modes: the opening mode including mineral-filled veins and barren joints, the shearing mode including faults and the mixed mode. Geometrically, they may occur at high angles, horizontal beddings or/and irregularly compacted planes in the reservoir. However, sealed or partially sealed joints are the most common type among many shale plays (Gale et al.

2014; Lorenz and Cooper 2020). The tensile failure mechanism against the minimum in-situ stress renders joints typically vertical or sub-vertical to the bedding and parallel to each other in the form of one or more fracture sets. From a standpoint of reservoir simulation, it is impractical to discretely mimic and simulate all geological structures in the reservoir. Only critical fractures, usually joints, that have certain abundance and serve as high-conductivity conduits dominating hydrocarbon flow are extensively focused on (Bourbiaux et al. 2005).

The self-affine nature found in many fracture systems supports a unique set of fractal parameters obtained from the limited sample to be scaled up in a model at larger scales. Based on a summary by Gutierrez and Youn (2015), the rest of this section will elaborate on a more comprehensive list of probability distribution frequencies (PDFs) that are commonly found in the natural field and thus used to describe natural joints fractal geometry in the modeling. **Table 2** summarizes all PDFs and references therein. PDFs can be obtained through deterministic observation or through statistical interpretation from in-situ data. For instance, natural fracture length profiles are found to follow power law distribution, lognormal distribution, exponential distribution and the first-order distribution based on the data from different plays. We will also briefly discuss how these distributions can be extrapolated to generate stochastic fracture models at multiple scales.

Table 2 PDFs for Statistical Characterization of Natural Fractures.

PDFs	Fracture Length	Fracture Location	Fracture Orientation	Fracture Aperture
Power law distribution	Yes (Segall and Pollard 1983; Heffer and Bevan 1990; Bonnet et al. 2001)	N/A	N/A	Yes(Snow 1970; Hakami 1995; Pyrak-Nolte et al. 1997)
Lognormal distribution	Yes (McMahon, 1971; Baecher et al. 1977; Barton 1978)	N/A	N/A	Yes (Tsang and Tsang 1990)
Exponential distribution	Yes (Robertson 1970; Call et al. 1976; Dershowitz and Einstein 1988)	N/A	N/A	N/A
First-order distribution	Yes (Davy et al. 1990; Bour and Davy 1999; Bour et al. 2002; Darcel et al. 2003)		N/A	N/A
Normal distribution	N/A	N/A	Yes (Long et al. 1982)	N/A
Fisher distribution	N/A	N/A	Yes(Fisher 1953; Priest 1993)	N/A
Poisson process	N/A	Yes (Priest and Hudson 1976; Baecher and Lanney, 1978)	N/A	N/A
Multiplicative cascade process	N/A	Yes (Schertzer and Lovejoy 1987; Meakin 1991; Darcel et al. 2003)	N/A	N/A

Fracture Length

Lognormal and exponential distribution of fracture length were mainly claimed by early researchers and are less favored currently because of power law's better physical significance (Barton and Zoback 1992). Pure power law for fracture length description was proposed based on many fields' data (Segall and Pollard 1983; Heffer and Bevan 1990). Its probability density is:

$$n(l) = \alpha l^{-a} \qquad eq.1(a)$$

in which, α is the constant fracture density term, $n(l)dl$ is the number of fractures having a length between l and $(l + dl)$, a is the power law exponent. Bonnet el al. (2001) collected data from many natural fields and discovered that the fracture length generally

followed a power-law distribution and emphasized the importance of upper and lower limits in the application. The maximum length l_{max} is a multiple of the minimum length l_{min}. By integrating the probability density, the constant term α can be expressed as **Eq.1(b)**.

$$\int_{l_{min}}^{l_{max}} n(l)dl = \int_{l_{min}}^{l_{max}} \alpha l^{-a} dl = 1$$

$$\alpha = \frac{1-a}{{l_{max}}^{1-a} - {l_{min}}^{1-a}} \qquad eq.1(b)$$

The cumulative distribution frequency (CDF) of fractures having a length between l_{min} and l can be represented by a uniformly random number F between 0 and 1 as **Eq.1(c)**. Thus, each fracture length l in a fracture model can be calculated in **Eq.1(d)** by combining **Eq.1(b)** and **Eq.1(c)**.

$$P(l_{min}, l) = \int_{l_{min}}^{l} n(l)dl = \frac{\alpha}{1-a}\left(l^{1-a} - {l_{min}}^{1-a}\right) = F \qquad eq.1(c)$$

$$l = l_{min} \times \{1 + F \times [(\frac{l_{max}}{l_{min}})^{1-a} - 1]\}^{\frac{1}{1-a}} \qquad eq.1(d)$$

This rule is also for applicable for fracture aperture distribution. Except power law, another widely employed length frequency distribution is the first-order model, a double power law relationship between fracture density and length, initially proposed by Davy el al. (1990). By integrating the PDF in **Eq.2(a)**, a total number of fractures $N(L)$ in the modeling area can be calculated as **Eq.2(b)**.

$$n(l) = \alpha L^{D_c} l^{-(D_l+1)} \qquad eq.2(a)$$

$$N(L) = \int_{l_{min}}^{l_{max}} n(l)dl = \frac{\alpha L^{D_c}}{D_l}\left({l_{min}}^{-D_l} - {l_{max}}^{-D_l}\right) \qquad eq.2(b)$$

where, D_l is the fractal dimension factor of fracture length, D_c is the fracture dimension factor of fracture center distribution, L is the domain size. $n(l)dl, a, \alpha$ are similar to those of power law. $a = D_l + 1$. l_{min} is the minimum fracture length and also a threshold, beyond which, the correlation of fracture center distribution and fracture length distribution is consistent over different fractal dimensions. While D_l is easily accessible by interpreting field fracture length profiles just as a in the power law, there are two approaches for deriving D_c from field information sources such as outcrop analogue data. The first one is based on the definition of a Pair Correlation Function $C_2(r)$ (Vicsek, 1992):

$$C_2(r) = \frac{2N_p(r)}{N(N-1)} = cr^{D_c} \qquad eq.2(c)$$

$N_p(r)$ is the number of pairs of joints whose distance is less than r, N is the total number of fractures and c is a constant term. D_c can be calculated as the slope of log $C_2(r)$ versus log r plot created on the basis of sampled datasets. Alternatively, if the availability of field datasets demonstrates a linear trend on a log-log scale for the distance dl between a fracture and its nearest neighbor whose length is larger than l as indicated by **Eq.2(d)**, the slope x will allow further calculation of D_c via **Eq.2(e)** (Bour and Davy 1999).

$$d(l) \propto l^x \qquad eq.2(d)$$

$$x = \frac{a-1}{D_c} = \frac{D_l}{D_c} \qquad eq.2(e)$$

Three constants α, D_c and D_l have critical impact on connectivity properties of two-dimensional (2D) fracture network. For 2D problems like this study, D_c is restricted to the range of [1, 2] and $D_l > 0$. D_c controls the degree of fracture clustering and when it approaches 2, fractures are uniformly distributed over the modeling area. D_l governs the

proportion of large fractures compared to smaller ones and when D_l approaches infinity, all fractures are constantly short. In most natural cases, $D_c > D_l$ is expected with D_c and D_l varying within the range of [1.5, 2] and [0.7, 1.8], respectively (Bour et al. 2002; Darcel et al. 2003).

Fracture Density

Two methods that are commonly implemented to generate fractal spatial density distribution for stochastic fracture models are the Poisson process and multiplicative cascade process. While the Poisson process is believed to be a feasible way to uniformly distribute random fracture centers in a 2D plane, multiplicative cascade process provides options to mimic the nature of fracture clustering in homogeneous reservoirs because it iteratively divides every parent domain into q subdomains. The probability of a parent domain P_i is randomly distributed to subdomains as well (Schertzer and Lovejoy 1987; Meakin 1991; Darcel et al. 2003):

$$\sum_{i=1}^{n} \frac{{P_i}^q}{(\frac{1}{sr})^{(q-1)D_c}} = 1 \qquad eq.3$$

where, sr is the scale ratio of parent domain length to subdomain length.

Fracture Orientation

Fracture orientation can be fully described by a strike along the horizontal plane and a vertical dip angle. As previously mentioned, fractures we are focusing on in this study are either vertical or sub-vertical. Therefore, the 3D orientation modeling is

simplified as a 2D strike distribution. In most cases, fracture strike can be easily measured from cores or outcrops. Fracture strike is often found to obey the Fisher distribution, whose probability density is (Fisher 1953; Priest 1993):

$$f(\theta) = \frac{K sin\theta e^{K cos\theta}}{e^{K} - e^{-K}}, \qquad 0 < \theta < \frac{\pi}{2} \qquad eq.4(a)$$

where, θ is angular deviation from the mean, K is Fisher's constant fixing the shape of deviation extent. The integral of the probability density is approximated as **Eq.4(b)**.

$$P(0,\theta) = \int_0^{\theta} f(\theta) d\theta = \frac{e^{K cos\theta} - 1}{e^{K} - e^{-K}} \qquad eq.4(b)$$

For large K, θ can be expressed as **Eq.4(c)** by ignoring e^{-K} term.

$$cos\theta \approx 1 + \frac{\ln (1 - P(0,\theta))}{K} \qquad eq.4(c)$$

in which, P is the cumulative distribution frequency of fracture having a strike between 0 and θ degree. Similarly, as it is in the power law, P can be represented by the random number F. Therefore, a set of fracture strike can be fully described as:

$$fracture\ strike = meanstrike + \theta$$

$$= meanstrike + cos^{-1}\left[\frac{l\,n(1-F)}{K} + 1\right] \qquad eq.4(d)$$

Normal distribution of fracture strike is often skewed and has less applicability (Long et al. 1982).

Fracture Aperture

The term 'fracture aperture' refers to the normal distance between two fracture surfaces that are either open or partially mineralized. At the very first, many studies

simplified fracture channels as two parallel and smooth plates separated by a constant aperture. However, later field data indicate that each fracture should have its own fracture aperture profile, or fracture roughness. Many of their aperture follow power law or lognormal distribution. The lognormally distributed aperture w can be described as the following expression (Tsang and Tsang 1990):

$$n(w) = \frac{1}{w\sigma\sqrt{2\pi}} e^{\frac{-(lnw-\mu)^2}{2\sigma^2}} \qquad eq.5$$

where, μ and σ are the expected value (or mean) and standard deviation of the fracture width natural logarithm, respectively. Tamagawa et al. (2002) claimed that fracture aperture was proportional to its length or diameter. Kim (2007) used the fractional Brownian motion (fBm, Voss 1988) to generate fracture apertures for fractal DFM models. Whichever the method is used to create fracture aperture profile, the Cubic Law is always used to determine the fracture permeability k_f. Correspondingly, flow conductivity is proportional to the fracture aperture raise to the power of three (Snow 1965). This Cubic Law is derived from Darcy's Law and Poiseuille's Law. Mathematically, the relationship between fracture permeability and fracture aperture can be described as below:

$$k_f \propto {w_f}^2 \qquad eq.6$$

Research Objective

In spite of the aforementioned industry sampling highlights, due to expensive costs and technology restrictions, it is extremely difficult to achieve field data sampling on such a scale in every target shale play. The investigation on fracture characteristics has been

focusing on regional, indeterministic or incomplete data collection such as analogous outcrops, cores, logs along the wellbore and microseismicity (Gale et al. 2014; Campbell et al. 2018). Extending these characteristics throughout the entire modeling domain remains challenging and requires a consistent methodology for integrating varieties of field data at different scales. Meanwhile, due to the incapacity of conventional continuum methods, there arises a need for proper DFN modeling methods to explicitly represent the heterogeneity of unconventional reservoirs. In addition, previous works on fractured reservoir simulation (Sun and Schechter 2015) have been using randomly generated DFN. Further validation of these reservoir simulation tools requires a geologically realistic DFN case.

In the context of research background and issues demonstrated above, we need to take advantage of available field data as much as possible to establish fractured reservoir models to mimic the fracture geometry and flow anisotropy dominated by fracture distribution in unconventional plays. Once the realistic fracture model is developed, it is necessary to apply it in numerical simulation for the purposes of validation, evaluation and optimization of reservoir production performance. In addition to field-based DFNs, conceptual DFN models can aid in testing the feasibility of new field development technology such as stimulation treatment design. The main problems we are going to address are summarized as follows:

1) What is the proper workflow to characterize and model the spatial distribution of natural fractures in shale reservoirs?

2) Is there a general methodology for integrating collected field data at different scales? How will the integrated data be applied as inputs in fracture modeling?
3) How many types of DFN models can be developed with the aforementioned workflow? How can we validate these models?
4) What are the applications of developed DFN models in field development?
5) Is it necessary to assign non-uniform aperture and permeability for each fracture in a field-scale model with great computation cost? How can we balance the computation costs of meshing, simulation processes and the explicitness of fracture description?

CHAPTER II

OVERALL WORKFLOW AND METHEDOLOGY OF DFN DEVELOPMENT

The overall workflow of this study is demonstrated as **Fig.2**. In order to complete the whole procedure, four elementary steps need to be taken: 1) generating two-dimensional (2D) fracture spatial distribution over the target reservoir domain; 2) defining the flow-related properties of the fracture system and reservoir matrix; 3) discretizing the developed fracture model with unstructured perpendicular bisector (PEBI) cells and exporting the meshed model and calculated connection list to a commercial simulator; 4) conducting reservoir simulations regarding different research demands. Different types of DFN models may focus on different steps, but they all follow the same procedure. The first three steps are realized by in-house software and the last step is completed by a commercial simulator. This study integrates and optimizes the previously existing techniques of discrete fracture generation, unstructured meshing algorithm and an output visualization module (Kim 2007; Sun 2016; Niu 2019) to constitute this more advanced in-house software named ‘iUnconventional’, which is coded with MATLAB.

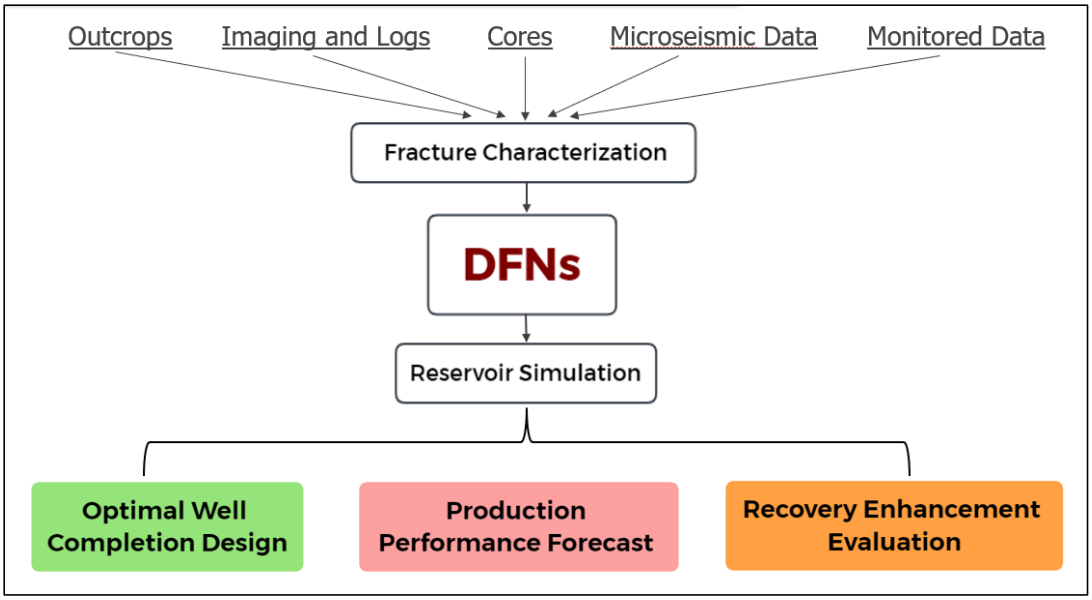

Figure 2 Workflow of DFN modeling and simulation.

Generation of Fracture Spatial Distribution

Generally, methodology of fracture generation can be divided into four categories, among which geologically represented DFN is the most straightforward approach. Its fracture distribution is either directly determined by geological sampled fracture patterns such as outcrop maps exposed on the surface, core data and image logs along the borehole (Niu 2019), or constrained by the location of microseismic events documented during hydraulic fracturing. The modeled natural fracture geometry of location, length and strike is supposed to be exactly the same as it in realistic fields. However, the size of the model is restricted to the exact size of the sampled domain accordingly. Otherwise, to build a field-scale model, the sampled fracture patterns must be representative enough to be extended over the whole reservoir by simple replication. Chapter 3 will present an outcrop-based DFN model and more details will be explained.

Synthetic or conceptual models are often designed to test the application of novel field development technology (Yu and Sepehrnoori 2018) rather than represent reality. In Chapter 4, a horizontal well model with multistage hydraulic fractures will be established to explore an optimal stimulation treatment plan for unconventional reservoirs. Natural fractures are ignored in these models.

Alternatively, the stochastic fracture model generated with statistical probability distribution of fracture parameters is another option. Deterministic observations of joint geology features are generally found to follow curtain statistical rules, as demonstrated in Chapter 1. Applying these rules to generate stochastic DFN model requires careful execution of field data interpretation as inputs. This study develops a 2D stochastic fracture generator, as one module of 'iUnconventional', based on the fractal DFN generation code of Kim and Schechter (2009). The main advantage of fractal DFN is scale independence, which allows flexible scales of modeling domain regardless of the measurement scale. In the meanwhile, more than one DFNs could be built with a single set of fractal dimension factors during the probability distribution process. Thus, sensitivity analysis and model validation are very important for this type of DFN model. In Chapter 5, the HFTS will be identified as the field case and necessary in-situ data will be collected at first. Then, we will investigate the use of multivariate data analysis and geostatistical simulation techniques to interpret field information at different scales. A one-stage stochastic fracture model will be established using the combination of statistical PDF method and direct in-situ distribution.

The fourth geo-mechanical approach is often used to mimic the propagation process of hydraulic fractures during stimulation. It will not be covered in this study for involving too many uncertainties concerning stratigraphy, petrophysical properties of formation and mechanical deformation mechanism.

As for hydraulic fractures, they grow on the basis of pre-existing natural fractures and part of natural fractures are activated by injection fluid during fracturing. No consensus has been reached on NF-HF interaction mechanism and corresponding HF propagation modeling method yet. Hence, this study will still make use of the simple bi-wing planar model to represent one hydraulic fracture cluster before a convincing and generally applicable model is brought up. Hydraulic fractures will directly overlay pre-existing natural fractures in the model if stimulation treatment is carried out in the reservoir, but they will differentiate from natural fractures in terms of assigned properties.

Definition of DFN Model Properties

All wells in unconventional reservoir models involved in this study are horizontal. All fractures are assumed to be vertical and thoroughly penetrate the formation thickness. In other words, fracture heights will be defined as the exact reservoir thickness and fracture shapes will be represented by rectangular planes perpendicular to the bedding. Thus, the full description of fracture geometry in DFNs contains fracture location, length, strike, aperture and height.

It is noteworthy that fracture aperture, compared with other geometric fracture parameters, is usually too minor to be detected on site or too difficult to be averaged with

a single value to represent the fracture roughness. Hence, the uncertainty analysis for fracture aperture is necessary. Previously DFN development tool (Sun and Schechter 2015) is able to define constant or non-uniform fracture aperture following lognormal distribution (Muralidharan et al. 2004), as depicted in **Fig.3 (b)** and **(c)**, respectively. To better reproduce the proportional correlation between fracture aperture and fracture size proposed by Tamagawa et al. (2002), this study supplements another way to generate fracture width profiles shown as **Fig.3 (d)**, where longer fractures would be assigned to larger apertures. **Fig.3(a)** is the zoom-out map view of fractures displayed in **(b)**, **(c)** and **(d)**. All fractures are surrounded by a layer of local grid refinement (LGR) to capture important flow behaviors between fractures and matrix, such as transient flow regime. Not only fractures but also intersections in the model can be refined. And the number of refinement layers and the size of refinement are user-defined.

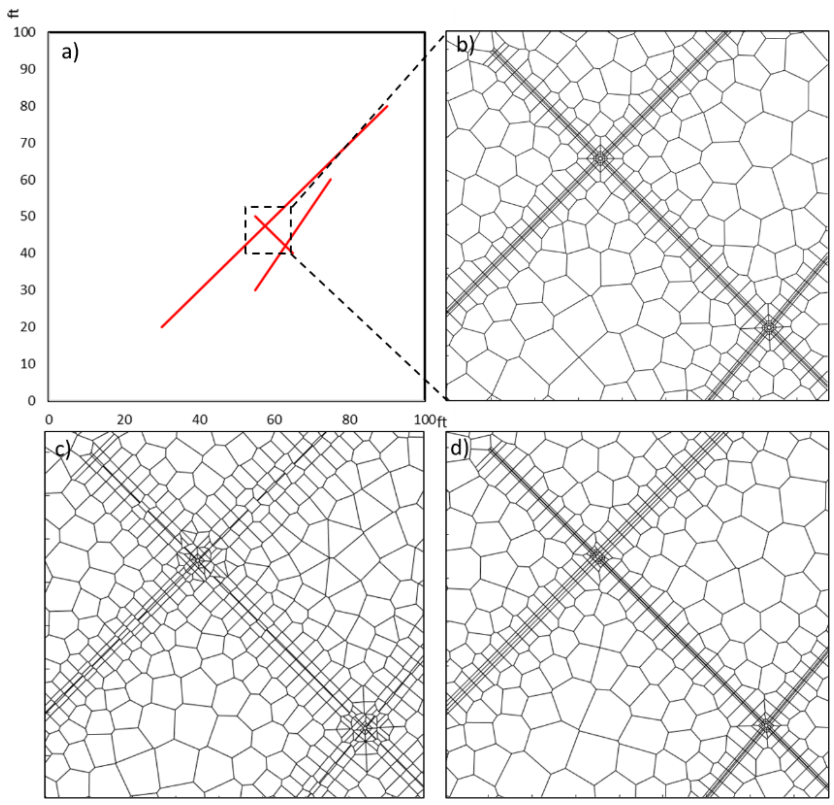

Figure 3 Multiple methods of fracture aperture assignment. a) 2D geometry of fractures represented by red lines; b) zoom-in view. All fractures have a constant aperture of 0.03 ft; c) zoom-in view. To mimic fracture roughness, the segments of each fracture are assigned with lognormally distributed apertures whose mean value is 0.03 ft; d) zoom-in view. Fractures have their own apertures that are constant along the fracture trace but different from each other. The apertures of the long to short fractures are 0.0706, 0.03 and 0.0118 ft.

Except this, the previous tool uses three permeability values including matrix permeability, NF permeability and HF permeability, to distribute permeability of each grid in the model. While the setting is reasonable regarding reducing simulation uncertainties, this study additionally enables each segment of fracture to have its own permeability calculated based on the Cubic Law, to better represent the fracture roughness and its impact on fluid flow.

Meshing of DFN Model

The spatial discretization of DFN models relies on the meshing process with unstructured grids, usually triangular or PEBI grids. For realistic and stochastic DFNs, special attention needs to be paid to deal with non-uniform aperture, clustering, low-angle intersections and LGR of fractures during discretization. Details about the optimization-based gridding approach employed in 'iUnconventional' can be found in Sun and Schechter (2015) but will not be elaborated here since it is not a job of this thesis. We will only briefly introduce the basic gridding settings for illustrative purposes.

The meshing process begins with the determination of fracture intersections and tips in the model. Each fracture is divided into multiple sub segments and fixed nodes are placed for each segment. These nodes represent the fracture aperture and LGR. Afterwards, flexible nodes are placed for matrix backgrounds and rearranged based on a certain optimized algorithm. Connecting all placed points can generate the 2D triangular mesh. The 2D PEBI mesh is the dual form of the triangular mesh. Some key parameters are supposed to be defined to control the mesh generation process such as initial grid size, fracture sub segment length, layer and size of fracture refinement, and incremental ratio of grid size.

Unlike conventional Tartan grids, unstructured grids are highly conformed with complex fracture geometry and thus greatly eliminate the grid-orientation effect. PEBI grid is also very flexible in terms of shape and size. The fine grids are set near fractures to capture the important flow behavior while coarse cells are used for background matrix to

reduce total cell numbers. However, the more complex the fracture system, the higher the CPU cost of DFN generation and discretization processes. Some research resorts to conventional continuum methods with DFN information implicitly incorporated in the modeling in search of high speed, large model scale and accuracy of multiphase flow (Dershowitz et al. 2000). In spite of that, this study firmly believes continuum models may work with homogeneous, conventional reservoirs but they would not become the appropriate modeling method for shale reservoirs under most circumstances. As a result, this study restricts the scales of intensively fractured models to the stage scale without compromising their explicitness and sets the NF-free synthetic models at the well scale to balance computation costs and clear representation of fractures.

Reservoir Simulation with Developed DFN

The developed and meshed two-dimensional DFNs like **Fig.3** will be extruded to 2.5D by specifying a reservoir thickness. Next, our software will export the fracture model and the calculated connection list to a commercial simulator, which in this study is Nexus@Haliburton. The connection list contains the pore volume of each cell, cell center depth, transmissibility between adjacent cells, and well-related information such as well index. Then, varieties of studies can be realized through reservoir simulation. The simulation results including pressure and saturation distributions for each time step can be visualized through a post-visualization module in the in-house software.

The impacts of fracture connectivity and conductivity on production can be understood via simulation. Conversely, as Tamagawa et al. (2002) proposed, calibrating a

static and geologically represented DFN with dynamic flow data via reservoir simulation is necessary to build a realistic fracture model. As in Chapter 5, a stage-scale DFN model developed based on the field information from the HFTS will be validated by a history match process with its actual production data

Besides, given that current primary recovery rates of shale plays are typically less than 10%, stimulation treatment needs to be optimized and recovery enhancement techniques need to be designed. The application of these technologies in the field can be preliminarily tested by reservoir simulation and eventually benefits hydrocarbon production and field development.

This study proposes a generally applicable workflow to illustrate the development and application of DFNs in fractured unconventional reservoirs. Different DFN cases will be elaborated in Chapter 3 to 5.

CHAPTER III

DEVELOPMENT OF THE OUTCROP DFN AND ITS APPLICATION IN SENSITIVITY ANALYSIS OF NATURAL FRACTURE APERTURE

To start with, this chapter develops an outcrop DFN model to explore the impact of natural fracture aperture on simulation production performance. It is also discussed whether the fracture roughness, more specifically non-uniform distribution of fracture aperture along the fracture trace, can be represented by a constant aperture in modeling. Later, to better reproduce the on-site production conditions, the outcrop model consisting of merely natural fractures is extended to a stage scale and five hydraulic fractures are incorporated. The individual and compound impacts of fracture aperture and permeability on the reservoir are analyzed using this larger model.

Development of Outcrop DFN Model

Outcrops are in-situ exposures of bedrock or ancient superficial deposits sampled from the surface for the purpose of geology analysis. The outcrop can be interpreted as a two-dimensional connectivity distribution of natural fractures in the reservoir. This study extracts the outcrop map of Bridger Gap in the Frontier formation and two sets of orthogonal natural fractures are observed, as displayed in **Fig.4**. Corresponding attributes of each set are summarized in **Table 3**. An image processor digitalizes the cracks as straight lines to represent fractures in the model in **Fig.5**.

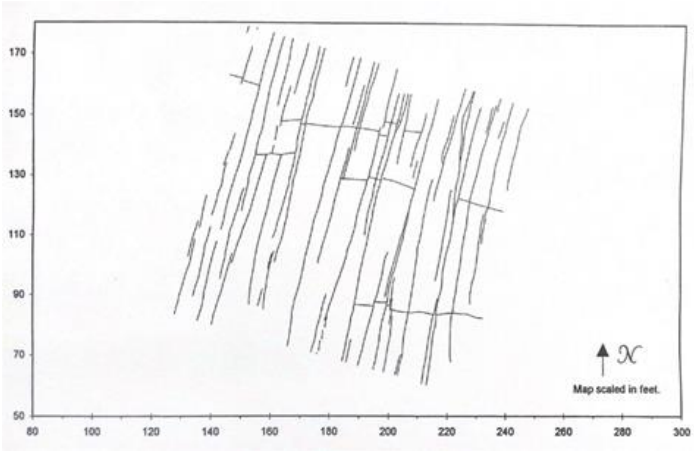

Figure 4 Outcrop map collected from the Frontier formation. Reprinted from Harstad et al. (1996).

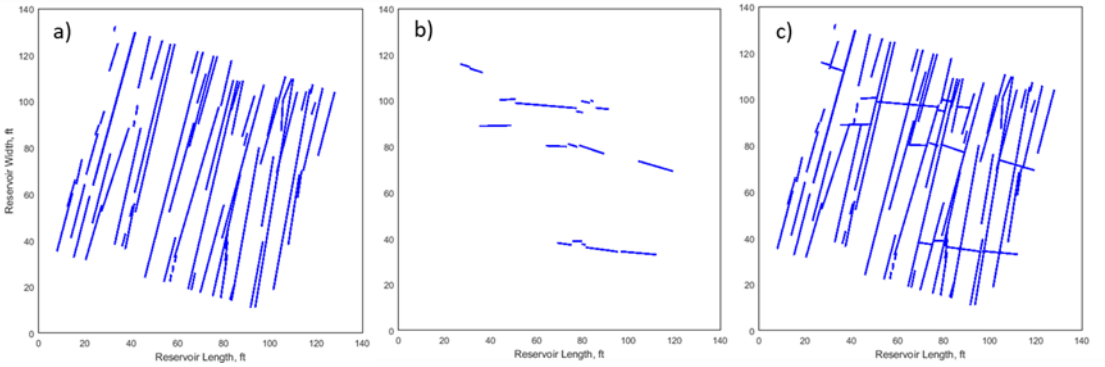

Figure 5 Digitized outcrop map. a) primary set of fractures; b) secondary set of fractures; c) both sets.

Table 3 Distribution Descriptions of Fractures in Bridge Gap Outcrop.

Description	Set 1	Set 2
Number of Fractures	69	18
Mean Strike, deg.	12.5	90
Min Fracture Length, ft	2.25	1.35
Max Fracture Length, ft	100.7	27

A reservoir thickness of 100 ft is assigned for the model. While natural fracture length, strike, height and location have been directly determined from the outcrop map,

the fracture width remains unknown. An initial value, 0.001ft, is assigned and sensitivity analysis of width will be conducted later in this chapter. With the optimization-based meshing algorithm, the model is meshed as **Fig.6**.

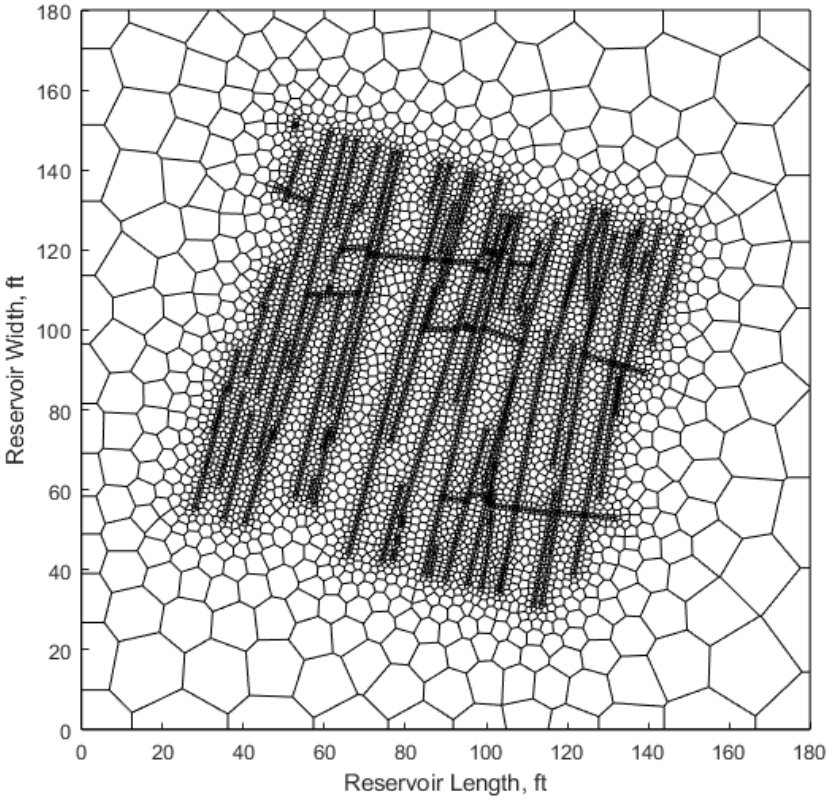

Figure 6 Two-dimensional natural fracture model meshed with unstructured PEBI cells.

Reservoir Simulation Settings

After the DFN model is established, it will be exported to the reservoir simulator, Nexus, to run simulations. **Table 4** lists the basic properties of the reservoir and fracture as input parameters for the simulation. Fracture permeability is calculated based on the

Cubic Law, which assumes the permeability is proportional to the square of fracture width. Note that listed hydraulic fracture properties are for the second model of this chapter.

Table 4 Basic Inputs of Reservoir and Fracture Properties for Simulation.

Properties	Value	Properties	Value
Reservoir Dimension, ft	180×180×100	**NF Porosity**	0.12
Datum Depth, ft	8000	**NF Permeability, mD**	Cubic Law
Pressure Gradient, psi/ft	0.6	**HF Aperture, ft**	0.03
Initial Pressure, psi	4800	**HF Porosity**	0.3
Saturation Pressure, psi	2364.7	**HF Permeability, mD**	4726.2
Matrix Permeability, mD	0.0005	**HF Half-length, ft**	87.5
Matrix Porosity	0.08	**HF Spacing, ft**	40
Initial Water Saturation	0.25	**Rock Compressibility, 1/psi**	1.00E-06

Given the fact that almost all unconventional reservoirs are intermediate to oil wet originally, this study utilizes an oil-wet relative permeability profile referred from Zhang (2020) as well as a black oil fluid model with PVT properties interpreted from the HFTS sample for multiphase simulation. They are tabulated in **Table 5** and **Table 6**, respectively.

Table 5 Summary of Relative Permeability and Capillary Pressure Curves. Data referred from Zhang (2020).

Water-oil Table			
Sw	**Krw**	**Krow**	**Pc, psia**
0.1	0	0.5	145.0377
0.125	0.0007	0.4546	9.76104
0.175	0.0062	0.3721	0.029008
0.2	0.0109	0.335	0
0.225	0.0171	0.3003	0
0.25	0.0246	0.2682	0
0.275	0.0335	0.2384	0
0.3	0.0438	0.2109	0
0.325	0.0554	0.1857	0
0.35	0.0684	0.1625	0
0.375	0.0827	0.1413	0
0.4	0.0984	0.1221	0
0.425	0.1155	0.1047	0
0.45	0.134	0.089	0
0.475	0.1538	0.075	0
0.5	0.175	0.0625	0
0.525	0.1976	0.0515	0
0.55	0.2215	0.0419	0
0.575	0.2468	0.0335	0
0.6	0.2734	0.0264	0
0.625	0.3015	0.0203	0
0.65	0.3309	0.0153	0
0.675	0.3616	0.0111	0
0.7	0.3938	0.0078	0
0.725	0.4272	0.0052	0
0.75	0.4621	0.0033	0
0.775	0.4983	0.0019	0
0.8	0.5359	0.001	0
0.825	0.5749	0.0004	0
0.85	0.6152	0.0001	0
0.875	0.6569	0	0
0.9	0.7	0	0
1	1	0	0

Oil-gas Table			
Sg	**Krg**	**Kro**	**Pc, psia**
0	0	0.5	0
0.05	0.001	0.375	0
0.175	0.0375	0.2785	0
0.2375	0.0844	0.2228	0
0.3	0.15	0.1866	0
0.3625	0.2344	0.11	0
0.375	0.25502	0.0833	0
0.425	0.3375	0.0517	0
0.4875	0.4594	0.0129	0
0.55	0.6	0	0

Table 6 Black Oil Fluid Model Interpreted from the HFTS Oil Sample. Data referred from NETL's Energy Data eXchange.

Saturated Table					
Pressure (psia)	Bo (RB/STB)	Oil Viscosity (cp)	Rs (MSCF/STB)	Bg (RB/MSCF)	Gas Viscosity (cp)
114.7	1.098387444	1.2103	0.047175704	25.9194381	0.0122
314.7	1.145687973	0.9898	0.128603524	9.216416631	0.0128
514.7	1.174181715	0.893	0.195156583	5.518263549	0.0132
1014.7	1.234869034	0.749	0.3362368	2.667353585	0.0144
1514.7	1.296204023	0.6392	0.482760873	1.730097558	0.0158
2014.7	1.361659037	0.5741	0.633118647	1.273099012	0.0174
2364.7	1.418611757	0.549	0.779182676	1.11	0.0182

Unsaturated Table			
Pressure (psia)	Bo (RB/STB)	Oil Viscosity (cp)	Rs (MSCF/STB)
2514.7	1.415190189	0.554	0.779182676
3514.7	1.395514178	0.5977	0.779182676
4087.7	1.386009515	0.6237	0.779182676
4514.7	1.379524295	0.6416	0.779182676
5014.7	1.372456755	0.664	0.779182676
5514.7	1.365865327	0.687	0.779182676
6014.7	1.359676094	0.709	0.779182676

Comparison of Non-uniform and Constant Fracture Width

Previous laboratory experiments (Sun and Schechter 2016) have observed that natural fracture width is non-uniform along its trace and generally follows lognormal distributions even under different in-situ stress. **Table 7** listed 3 sets of parameters of three different lognormal distributions, where μ and σ are the expected value and standard deviation of the aperture's natural logarithm.

Table 7 Summary of 3 Different Lognormally Distribution Cases.

Case Description	Mean	μ	σ	Cum Oil, Mstb	Recovery, %
Log0 (no in-situ stress)	0.0012156	-6.853817912	0.53166403	1.98	7.25
Log1 (under 500 psi)	0.0006496	-7.621724608	0.751750864	1.669	6.11
Log2 (under 1000 psi)	0.0005066	-7.960138588	0.863007786	1.555	5.69

These three lognormally distributed aperture profiles are used to generate 3 aperture profiles for the outcrop DFN model in **Fig.6**. The zoom-in view of fracture apertures is similar at it is in **Fig.3(c)**. The probability density of apertures generated by our software 'iUnconventional' for 3 different cases are collected and displayed in the **Fig.7** below.

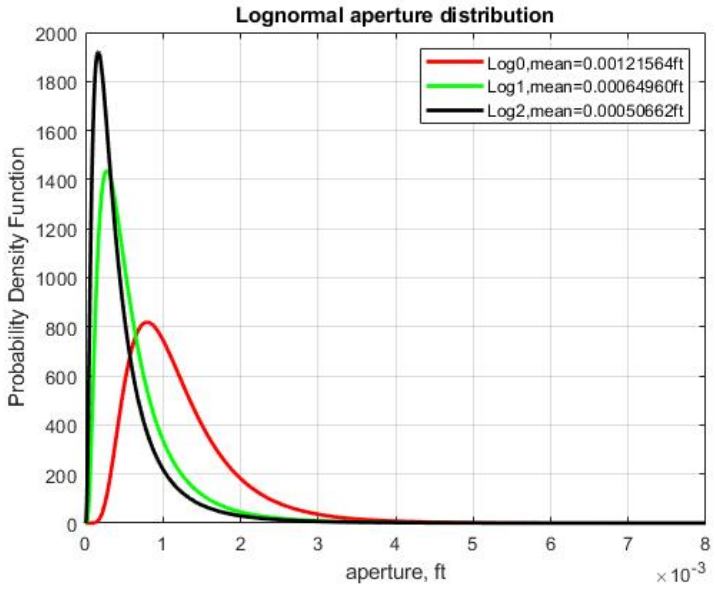

Figure 7 Non-uniform aperture distributions under three different overburden pressures generated for 3 cases.

A constant bottomhole flowing pressure (BHP) of 500 psi is set as the simulation constraint. The cumulative oil production results after 5-year depletion are depicted in **Fig.8**. As the overburden stress increases, fractures close, resulting a decrease in cumulative oil production.

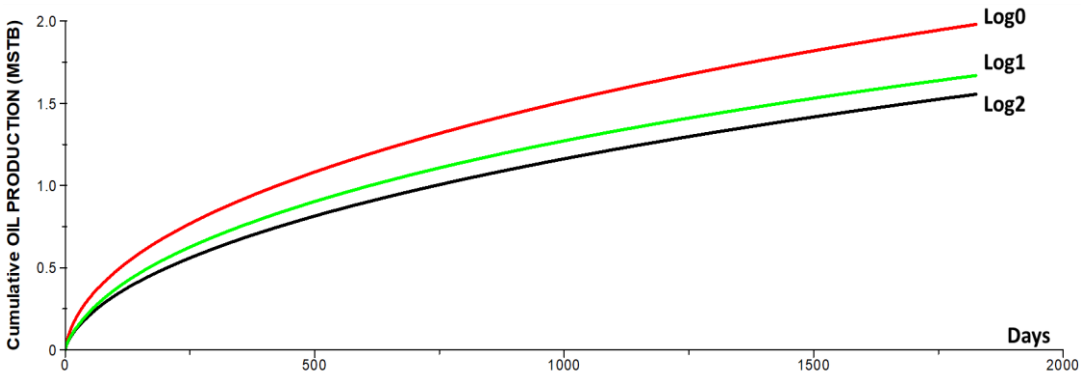

Figure 8 Cumulative oil production results of various lognormal distribution cases of fracture aperture.

In reservoir simulation, however, the width of all natural fractures is often represented by a single value to reduce the computational cost especially in large models or to reduce the number of adjustable parameters during the history matching process. Next, this study analyzes the rationality of averaging the fracture roughness as a single constant value in the simulation.

A case with a constant aperture of 0.001387 ft, the arithmetic average of lognormally distributed apertures in case 'Log0', is developed based on the same model in **Fig.6**. The same production simulation is performed and the result is compared with the result of case 'Log0', as shown in **Fig.9**. Cumulative production of this case turns out

to be much higher than that of case ‘Log0’. Apparently, the irregular shape of fracture channels has a detrimental effect on hydrocarbon mobility and could not produce as well as the arithmetically averaged, constant width case.

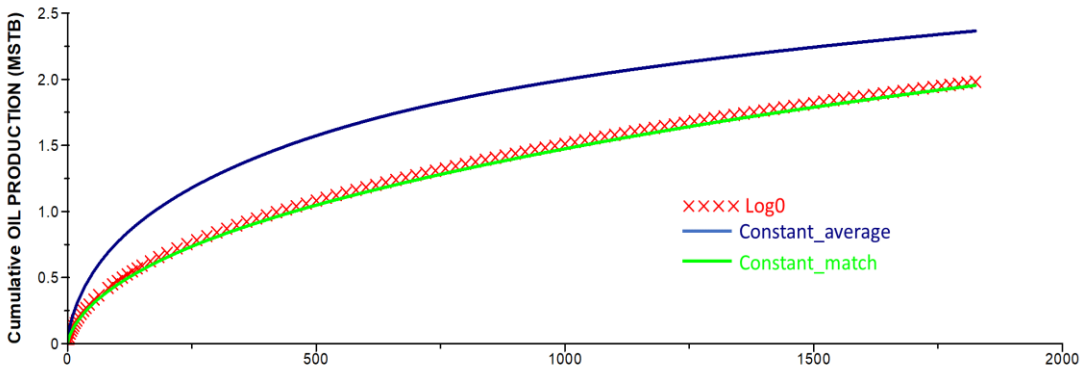

Figure 9 Cumulative oil production results of three cases. Red cross line indicates the case with lognormal distributed fracture width. Blue line indicates a constant width case and its width 0.001387ft is the arithmetic average of the lognormal distribution case. Green line indicates another constant width case in order to match the lognormal case and its width is 0.0008ft.

The green curve in **Fig.9** is another constant-width case. Since the average value is unable to represent fracture roughness, this study further tests other constant apertures for the purpose of matching the lognormal distribution case. Finally, a constant width of 0.0008 ft is found to be close enough to and to be able to mimic the ‘Log0’ case in terms of the cumulative production.

The cases we have performed so far demonstrate the importance of non-uniform distribution of fracture aperture to reservoir production and the necessity for it to be explicitly represented in modeling. However, when a faster computation speed or a larger model size are required, a constant fracture aperture may also represent the fracture

roughness for simplicity. Particularly, this constant aperture is expected to be smaller than the arithmetic mean of the non-uniformly distributed apertures.

Sensitivity Analysis of NF Width and Permeability

In this section, three different groups of cases are designed to analyze the sensitivity of field-scale production performance to fracture width and fracture permeability. In order to constitute a larger model on the basis of a limited outcrop sample, Sun (2016) extended the collected outcrop pattern in both reservoir length and width directions. In the same way, this study rotates and duplicates the pattern in **Fig. 5(c)** to constitute a 2-by-2 pattern matrix in a 245×260×100 cubic feet model. One fracturing stage with five hydraulic fractures perpendicular to the well trajectory is also incorporated, as displayed in **Fig.10(a)**. Similarly, 'iUnconventional' completes the meshing process. The meshed 2D model and extruded 2.5D model are displayed in **Fig.10(b)** and **10(c)**, respectively.

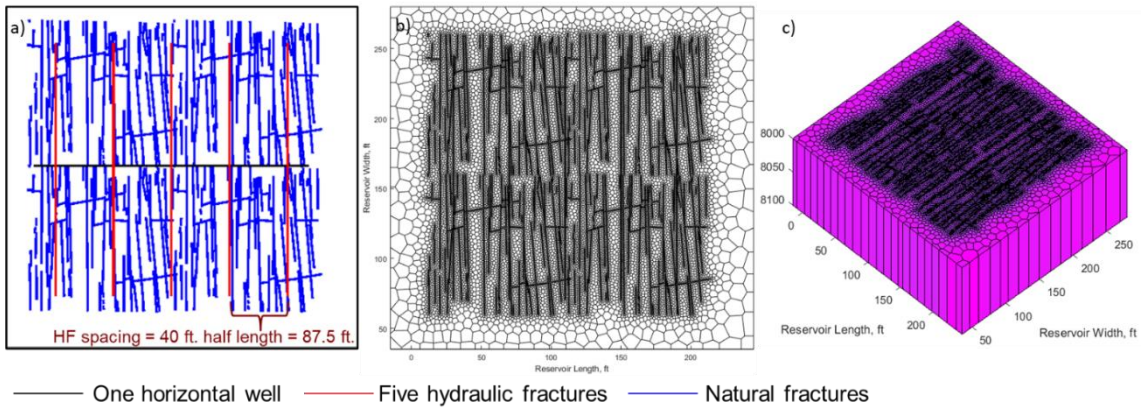

Figure 10 Development of the outcrop model. a) 2D one-stage model. The well trajectory is indicated by the black line, HFs are indicated by red and NFs are indicated by blue lines; b) 2D one-stage model meshed with unstructured PEBI cells; c) extruded 2.5D model. The reservoir thickness is 100ft.

According to the previous section, constant fracture width is acceptable for the simulation of large-scale models, hence this section will use constant apertures in all cases. An initial value of 0.001 ft is assigned for the base case 1. The natural fracture width, permeability, conductivity and simulated oil recovery of all these cases are tabulated below. The properties of hydraulic fractures have been listed in **Table 4** and all the other simulation settings are the same as those of **Table 4**. Similarly, the BHP is set as 500 psi during the primary depletion process.

Table 8 Three Groups of Cases of Fracture Aperture Sensitivity Analysis.

Group Description	Case	NF Width w_f, ft	NF Permeability k_f, md	Conductivity, md-ft	Recovery, %
1 – varying w_f & k_f	2	0.0005	0.9675	0.00048375	10.62
	1	0.001	3.87	0.00387	11.36
	3	0.01	387	3.87	11.98
2 – varying w_f & constant k_f	4	0.0005	3.87	0.001935	11.21
	1	0.001	3.87	0.00387	11.36
	5	0.01	3.87	0.0387	11.36
3 – constant w_f & varying k_f	6	0.001	0.9675	0.0009675	10.63
	1	0.001	3.87	0.00387	11.36
	7	0.001	387	0.387	13.33

The first thing we should notice is that recovery factors of all 7 cases in **Table 8** are greater than those of NF-only cases in the previous section due to the aid of stimulation treatment. In group 1, the natural fracture width varies from 0.0005 ft to 0.01 ft and the fracture permeability is calculated according to the Cubic Law. The cumulative oil production of three cases is depicted in **Fig.11**. It is obvious that as the fracture width increases, fracture permeability increases and cumulative production increases consequently.

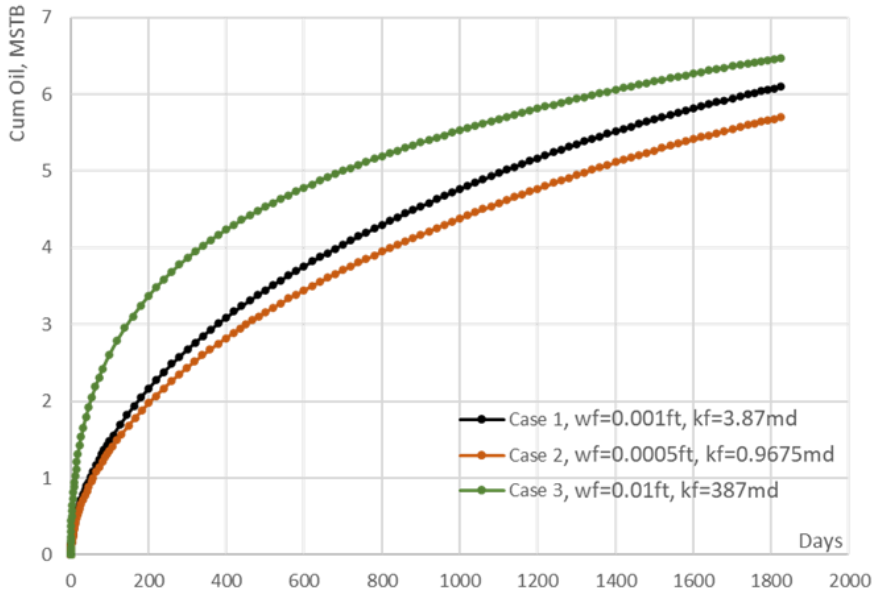

Figure 11 Cumulative oil production results of group 1.

In order to explore the separate contribution of fracture width and permeability to production, they are assumed to be independent of each other in group 2 and group 3. As it is shown in **Fig.12** for group 2, when the fracture permeability remains constant, a larger fracture width leads to a faster production rate but the cumulative production results are very similar in all cases. For instance, although the fracture width of case 5 is an order of magnitude higher than that of case 1, the recovery difference between them is negligible, being 11.365% and 11.362%, respectively. Facts prove that the key role of fractures in the reservoir is to provide high-speed flow paths instead of storing extra hydrocarbons.

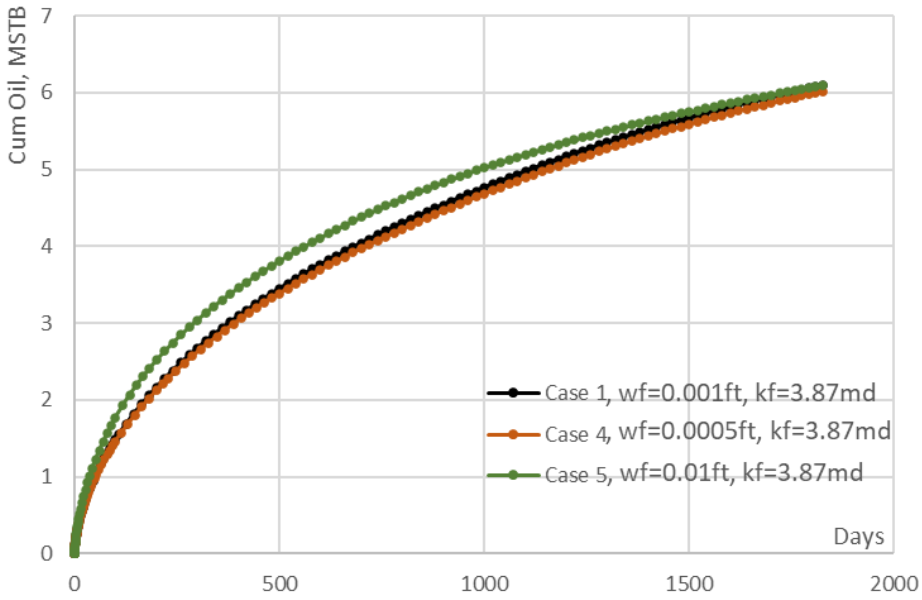

Figure 12 Cumulative oil production results of group 2.

As for group 3, fractures apertures are kept constant and a significant increment in production can be observed as fracture permeability increases in **Fig.13**.

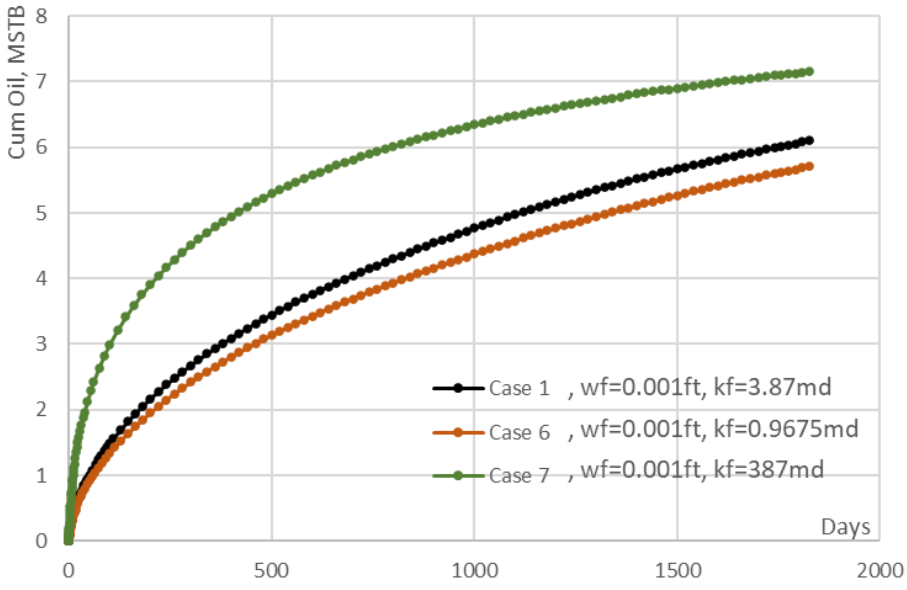

Figure 13 Cumulative oil production results of group 3.

Based on these 7 cases, it can be concluded that in each group, cumulative oil production and fracture conductivity, the product of fracture width and permeability, is positively correlated. Furthermore, unconventional reservoir production is not very sensitive to fracture width itself. However, in nature, fracture width often determines fracture permeability, which has direct and significant impact on reservoir production performance. An appropriate representation of fracture permeability in modeling is more important than the direct measurement of fracture apertures in the field.

CHAPTER IV

DEVELOPMENT OF THE SYNTHETIC DFN FOR OPTIMAL STIMULATION DESIGN

In regard to the ultra-low permeability and tiny pore size of unconventional plays, current field development technologies of horizontal drilling, well spacing and multi-stage hydraulic fracture stimulation have resolved around maximizing stimulated reservoir volume (SRV) and high-conductivity fracture networks to aid subsurface fluid transport and hydrocarbon production. However, the primary recovery of most shale plays still remains unsatisfactory. Therefore, in this chapter, conceptual models consisting of horizontal wells and multistage hydraulic fractures are designed to explore the optimal stimulation treatment and its application in the field.

Analysis of Uniform Fracturing Pattern

In unconventional reservoirs, horizontal wells are stimulated by multiple stages of hydraulic fracturing. Typically, each stage has two to eight perforation clusters orthogonal to the well trajectory (Cipolla et al. 2011), and each cluster is equally injected and propped with the same amount of stimulation fluids, resulting in an even distribution of hydraulic fractures along the well. For instance, the map view of a typical model consisting of a horizontal well and 6 stages of hydraulic clusters is illustrated in **Fig.14**. One stage has 4 perforated clusters and each cluster is represented by a rectangle in 3D view or a straight line in 2D view. The occurrence of natural fractures is ignored in this model.

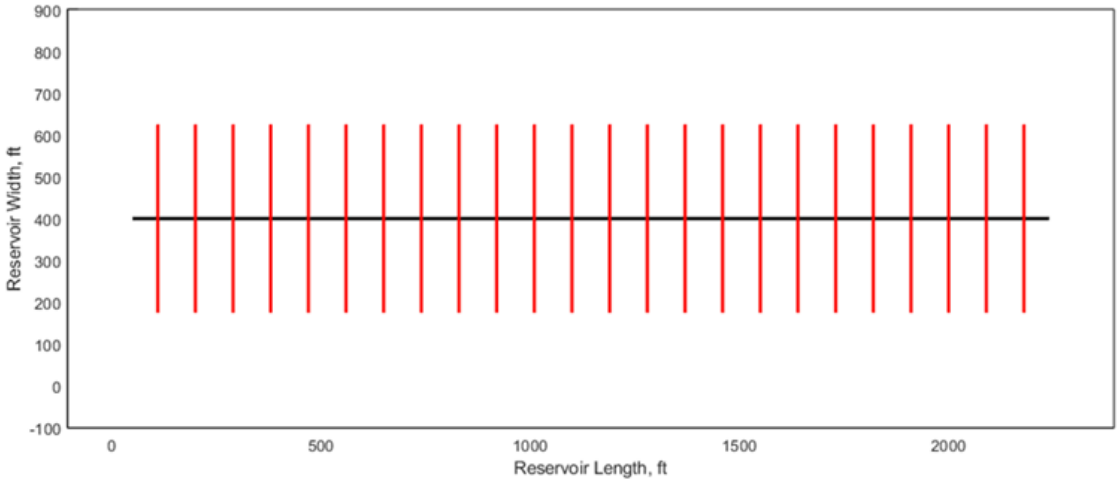

Figure 14 Map view of a basic reservoir model (case 1), including 6 fracturing stages and 4 clusters per stage that are uniformly distributed. The well trajectory is denoted as the black line and HFs are denoted as the red lines.

For such a case, a simple primary depletion test at a constant bottomhole flowing pressure (BHP) of 800 psi is performed for 10 years. All inputs of model properties are tabulated in **Table 9** and other simulation settings are the same as those of Chapter 3. The simulation result, a pressure distribution map, is demonstrated in **Fig.15**.

Table 9 Basic Inputs of Model Properties for Simulation.

Parameters	Value	Parameters	Value
Reservoir Dimension, ft	2500×1000×200	**Lateral Length of Well, ft**	2190
Datum Depth, ft	8000	**Number of Stages**	6
Pressure Gradient, psi/ft	0.6	**Cluster Number per Stage**	4
Initial Pressure, psi	4800	**Total HF Half-Length, ft**	10800
Saturation Pressure, psi	2364.7	**Cluster Spacing, ft**	90
Matrix Permeability, mD	0.0005	**Stage Spacing, ft**	360
Matrix Porosity	0.08	**HF Aperture, ft**	0.03
Initial Water Saturation	0.25	**HF Porosity**	0.3
Rock Compressibility, 1/psi	1.00E-06	**HF Permeability, mD**	4726.2

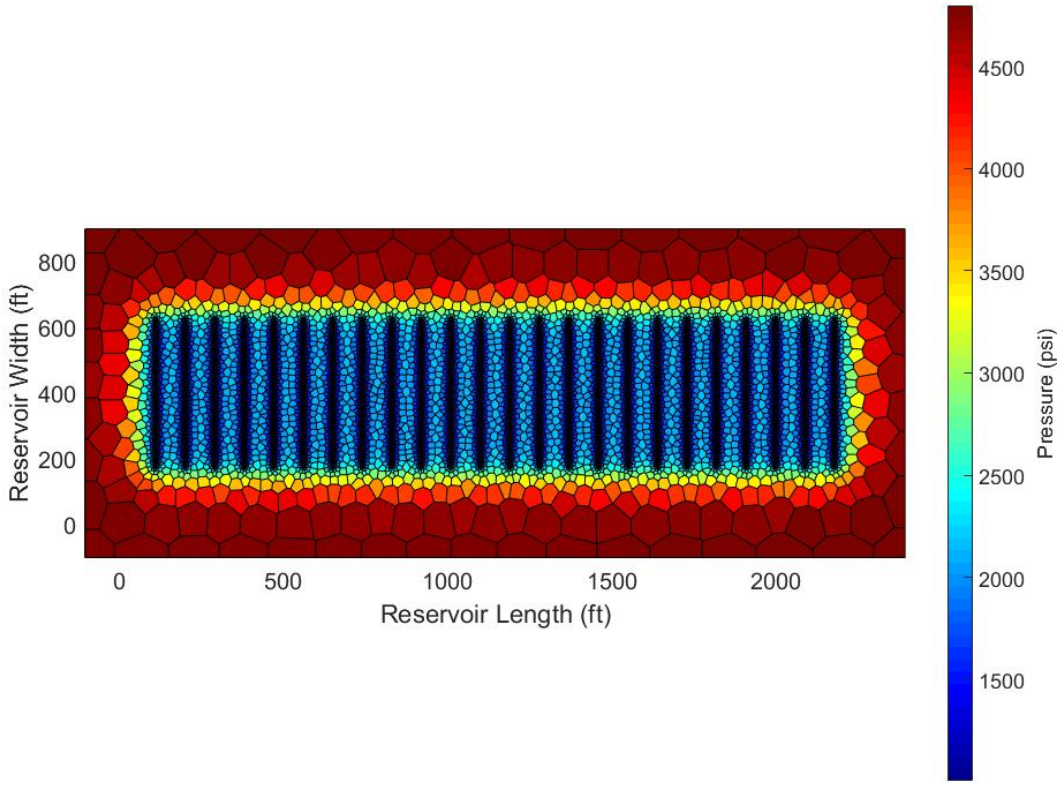

Figure 15 Pressure distribution diagram of case 1. Dark red indicates the area of high pressure and dark blue indicates the area of low pressure.

As can be found in **Fig.15**, the low-pressure region is strictly limited by the extension of generated HFs while the large matrix area remains barely exhausted even after 10 years' production. Its recovery rate is as low as 4.91%. As a result, there arises a need for an optimal design of fracturing pattern that is able to produce the greatest amount of oil at the same stimulation cost, which is defined as the total injection volume with all technical and practical difficulties of execution ignored and with leak-off coefficients assumed to be identical in this study. The simulation cost can be further represented as the total HF half-length and the reason will be explained as follows.

The dimensionless fracture conductivity F_{CD} is defined as:

$$F_{CD} = \frac{k_f w_f}{k_m x_f}$$

where, k_f is fracture permeability, w_f is fracture width, k_m is matrix permeability and x_f is fracture half-length. When $F_{CD} > 300$, fractures are taken as infinitely conductive. Given the vast difference in permeability between the propped hydraulic fractures k_f and fairly tight shales k_m, all hydraulic fractures in our models are considered to have infinite conductivity and thus reservoir production will be insensitive to fracture width. In order to verify this statement, three scenarios with different fracture widths for the basic model in **Fig.14** are established. Their fracture permeability is determined according to the Cubic Law. By repeating the 10-year depletion simulation, three cases having different fracture widths yield similar cumulative oil production results, as displayed in **Fig.16**. Therefore, it is reasonable to claim that total costs for stimulating a well can be simplified as the total propagated HF length of the model. In this respect, the next section will discuss if the uneven distribution of fracture length will improve oil recovery at the same stimulation costs.

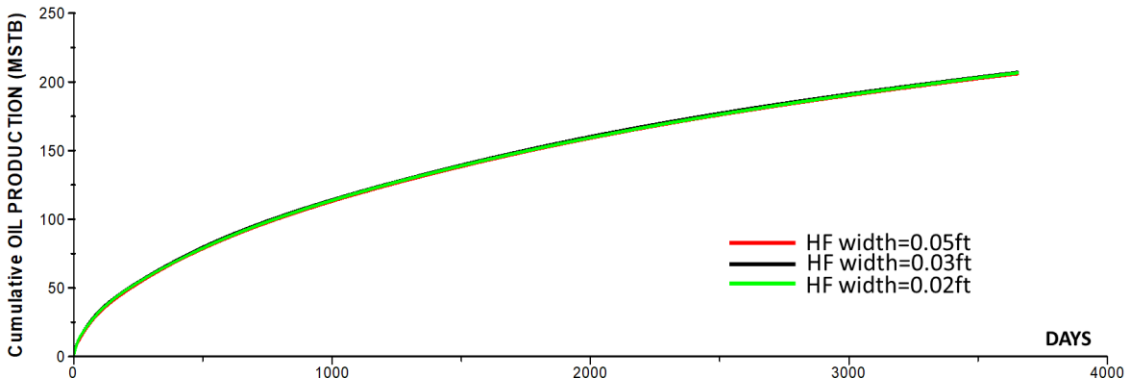

Figure 16 Fracture width insensitivity tests. Three cases of different fracture conductivity yield similar cumulative oil production results after 10 years' depletion.

Development of Uneven Distribution of Fracturing Pattern

In this section, eight synthetic models with varying individual half-lengths and the same total half-length (10800 ft) are designed, upon which the same 10-year depletion test performs. The fracture length distribution of all cases and their simulated production results are listed in **Table 10**. All fracture widths are set as a constant value of 0.03 ft in accordance with the analysis demonstrated above. While other research has investigated the variation of HF half-length within a stage (Yu and Sepehrnoori 2018), more scenarios are taken into account in this study in which the HF fracture length can vary along the whole well trajectory.

Table 10 Summary of Fracture Length Distribution of 9 Cases and their Simulated Production Results.

Case	HF Half-length, ft	Cum Oil, Mstb	Recovery Factor, %
1	225*24	206.963	4.91
2	(350+100)*12	217.926	5.17
3	(350+100+100+350)*6	213.347	5.06
4	(100+350+350+100)*6	212.228	5.04
5	(350*4+100*4)*3	209.302	4.97
6	(360+270+180+90)*6	211.915	5.03
7	(360+270+180+90)*3+(90+180+270+360)*3	211.968	5.03
8	104+126+148+170+192+214+236+258+280+302+324+346*2+324+302+280+258+236+214+192+170+148+126+104	206.735	4.91
9	346+324+302+280+258+236+214+192+170+148+126+104*2+126+148+170+192+214+236+258+280+302+324+346	207.699	4.93

Except for the basic case 1, the other 8 cases are divided into two groups. In group 1, case 2 to case 5 in **Fig.17** describe different combinations of 12 long fractures (half-length = 350 ft) and 12 short fractures (half-length = 100 ft) that are alternatively distributed. The simulation results show that the different distribution of hydraulic fractures yields different recovery rates. Recovery ranking of group 1 is: case 2 > case 3 > case 4 > case 5. It can be observed that the high switching frequency of long fractures and short fractures in the model is conducive to the cumulative oil production. More specifically, case 2 has the highest switching frequency between long and short fractures. Case 3 and 4 have the same switching frequency and case 5 switch very slowly between long and short fractures. The switching frequency ranking determines their recovery ranking. The reason why case 3 is slightly better than case 4 is that case 3 starts and ends with a long fracture while case 4 starts and ends with a short one. This only difference between them allows case 3 to surpass case 4 in terms of oil recovery.

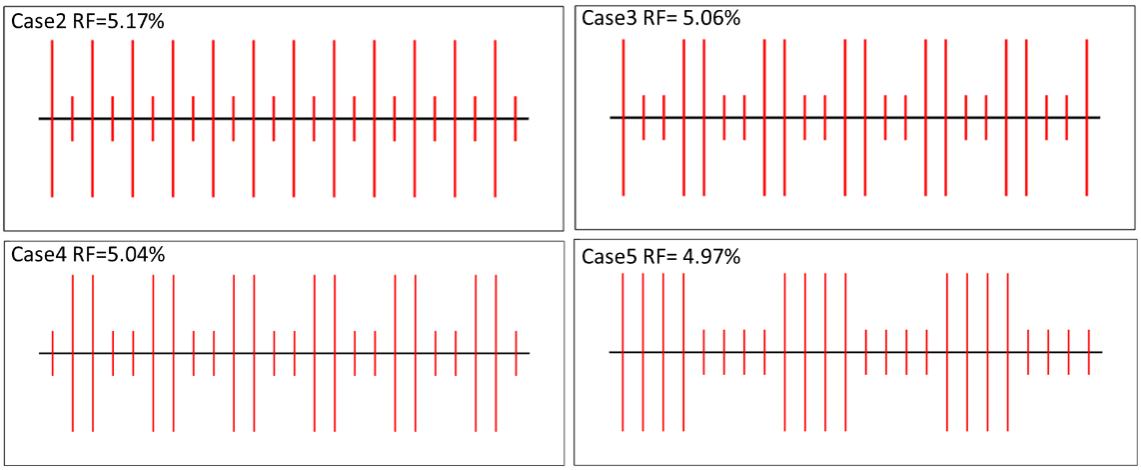

Figure 17 2D schematic of synthetic case 2-5 having the same total HF length. Well trajectories are indicated by black lines and hydraulic fractures are indicated by red lines. Long fractures and short fractures are alternatively distributed.

In **Fig.18**, case 6 to case 9 depicts the gradual change in fracture length within one stage (case 6 and 7) and the whole well (case 8 and 9). Recovery rates of these 4 cases are ranked as: case 7 > case 6 > case 9 > case 8. The gradual variation in fracture length of case 8 and 9 seems to have no strength and should be avoided in practice. Case 7 performs better than case 6 because its symmetrical distribution places long fractures at both the beginning and end of the horizontal well.

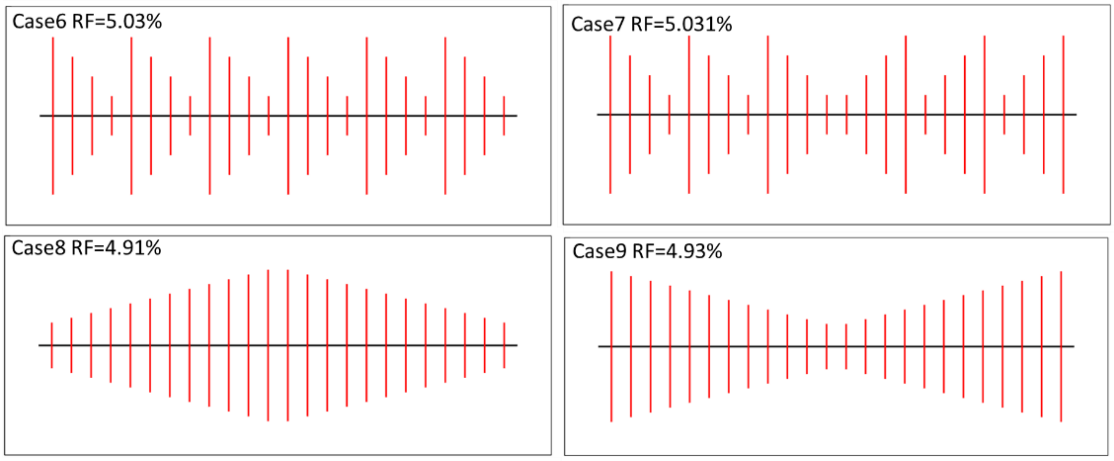

Figure 18 2D schematic of synthetic case 6-9 having the same total HF length. Well trajectories are indicated by black lines and hydraulic fractures are indicated by red lines. Fracture lengths are gradually changed within a stage or along the whole well.

The recovery ranking of all 9 cases is: case 2 > case 3 > case 4 > case 7 > case 6 > case 5 > case 9 > case 8 > case 1. The comparison between them is quite enlightening, based on which we conclude some general principles of optimal stimulation design that can be applied in industrial practice to improve the production in unconventional reservoirs:

1) First and foremost, all non-uniform patterns of hydraulic fractures perform better than the conventional uniform distribution in base case 1, in regard to oil recovery. In other words, the evenly spaced simulation strategy widely employed in the majority of actual fields may be the simplest but worst option we have. It is very important to design better perforation tools and pumping schedules in accordance with the results obtained through this study.

2) Creating large SRV boundaries is critical. Obviously, the perforations/stages at the toe and heel of a horizontal well have the chance to get contact with greater volume of original oil in place (OOIP) relative to hydraulic fractures in the center. When the total amount of injection fluids is fixed, priority should be given to the first and last perforations/stages to create large boundaries of the stimulated area. For example, case 3 and 4 have similar fracture length distribution, but the recovery factor of case 3 is higher than that of case 4 because it places longer fractures in the first and last perforations. The same conclusion can be drawn from the comparison between case 8 and 9 whose hydraulic fracture lengths are identical, but the case with longer fractures located in the center yields worse production.
3) It is also worth noting that operators should avoid leaving large intact areas unstimulated. Take the first group as an example, there are twelve 350-ft long and twelve 100-ft short fractures in each model. However, the ranking of their intact unstimulated regions is: case 5 > case 4 = case 3 > case2, so is their recovery raking except that the recovery of case 3 is slightly higher than case 4 because of principle No.2. Amongst all 9 cases, case 5 and 9 have very large and intact areas unstimulated, as demonstrated in **Fig.19**, making them unfavorable fracturing patterns.

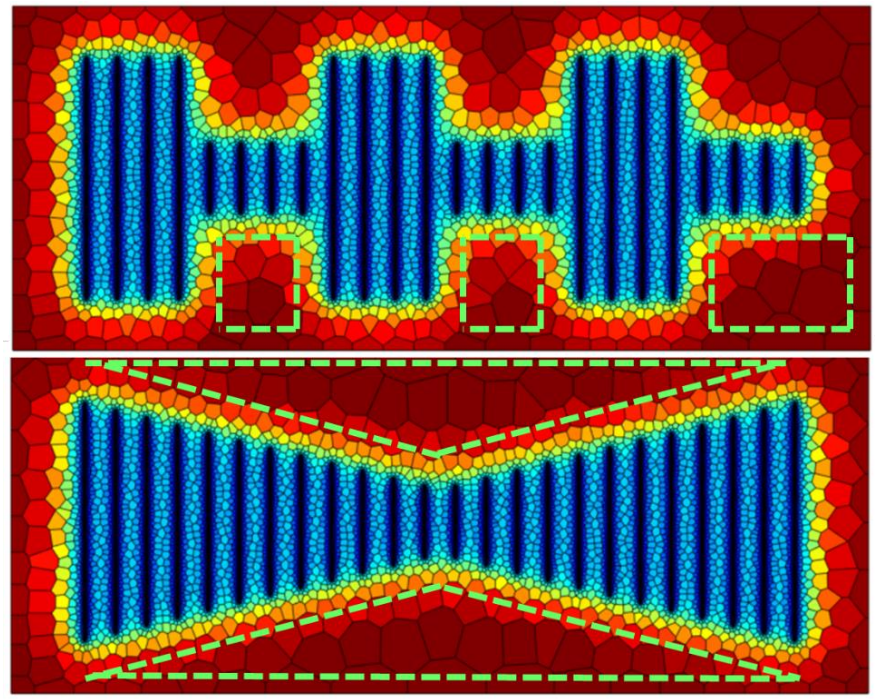

Figure 19 Pressure distribution maps of case 5 and case 9 after 10-year depletion. Intact unstimulated areas are indicated by green dashes.

Although the relative ranking of these 9 cases may slightly change in accordance with specific situations such as different density of pre-existing natural fractures, higher reservoir permeability and porosity, different hydraulic fracture spacing and model size etc., three principles summarized above are found to be repeatable and universal. For instance, in Yu and Sepehrnoori's study, five non-uniform hydraulic fracture patterns within one perforation stage under the same total fracture length are investigated, as **Fig.20** displays. The shale gas recovery ranking of these five patterns is: pattern 5 > pattern 4 > pattern 3 > pattern 2 > pattern 1, which are consistent with our results. First, all the other 4 cases perform better than the uniform case 1. In addition, long fractures placed for the

first and last fractures and small unstimulated zone in case 5 make it stand out among 5 patterns in terms of total oil production.

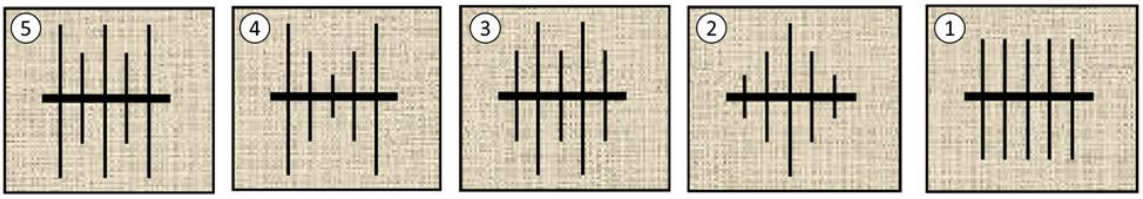

Figure 20 Five different hydraulic fracture patterns within one perforation stage under the same total fracture length of 5000ft. Reprinted from Yu et al. (2014).

Quantitative Analysis of Cluster Production

According to the analysis illustrated above, case 2 is the optimal fracturing mode in this study. If the number of perforation cluster per stage is odd rather than even, long fractures can then be placed at both the beginning and end of a well. In this way, cumulative production would be expected to be even higher.

After the optimal design is determined, the partial contribution of each fracture to the total production is still unknown. To the best knowledge of this study, no previous research has been conducted to quantify the production of a single perforation. Hence, for the purpose of better understanding how specifically non-uniform stimulation treatment enhances hydrocarbon flow rate, this study quantifies the perforation production of the worst case 1 and best case 2 from the previous section. **Fig.21** demonstrates the ratio of single perforation production to the total cumulative oil production in case 1. It can be observed that with the exception of the 1st and 24th perforations which have higher

contribution rates due to their greater exposure with OOIP, all the other perforations evenly produce around 4.14% of the total cumulative production.

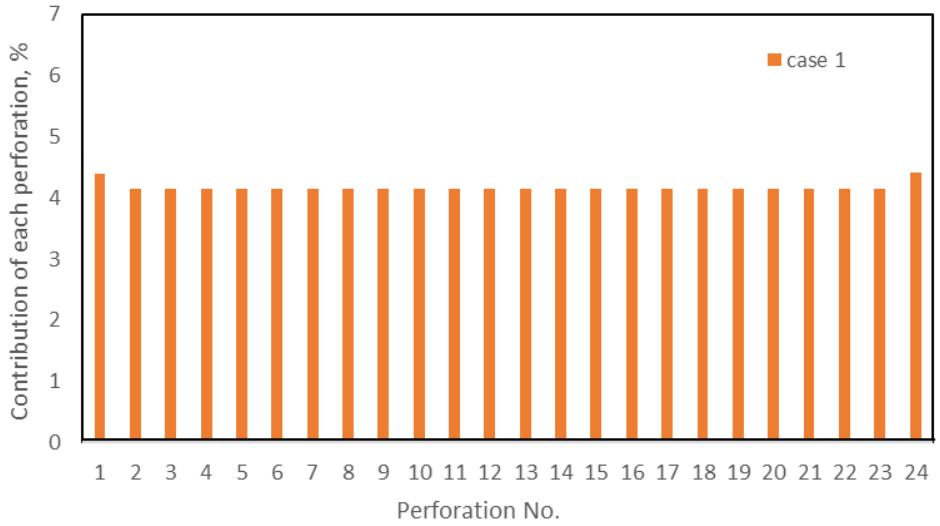

Figure 21 Quantitative analysis of the production contribution of individual perforations for basic case 1.

In the same way, the khaki bars in **Fig.22** quantifies the perforation production of the optimal fracturing pattern, case 2. The giant difference in cluster production between case 1 and case 2 manifests that in unconventional plays, perforation productivity is strictly and positively correlated with fracture length. The reason we specify it as 'unconventional' is that, by performing the same numerical simulation on case 2 in conventional reservoirs, we observe a distinctive perforation production profile, just as the blue bar in **Fig.22** shows. The conventional reservoir here means greater permeability and larger porosity, as they are assigned in our simulation with values of 10 mD and 15%, respectively. Due to the fast fluid flow rate in the matrix, explicit representation of fracture geometry in conventional reservoir models is not as important as it is in unconventional

reservoir models. The outer fractures in contact with greater amounts of matrix volume produce more hydrocarbon while those in the middle having to compete OOIP with other fractures produce less hydrocarbon, regardless of the fracture length variation along the horizontal well.

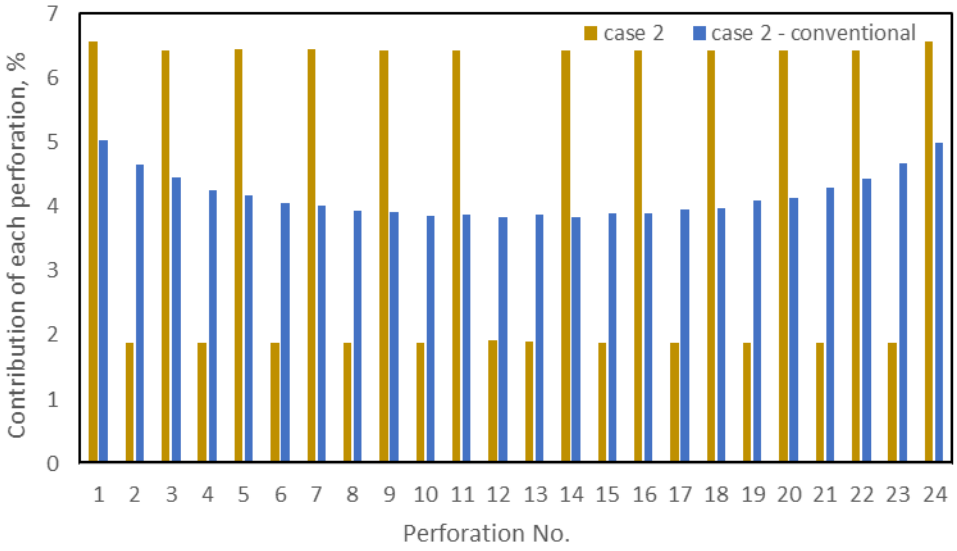

Figure 22 Quantitative analysis of the production contribution of individual perforations for case 2 in conventional and shale plays, respectively.

The conceptual model developed in this chapter may not necessarily reflect the actual field conditions as many assumptions and simplifications have been made on them. But the objective of chapter is not to represent reality but to compare different stimulation patterns. The insights gained from this simple model reveal two main facts. On the one hand, an optimal stimulation design is crucial to production efficiency in shale reservoirs as the induced fracture channels of high conductivity dominate the fluid flow. Operators should aim at creating non-uniform hydraulic fracturing patterns. On the other hand, since

the spatial distribution of fracture has tremendous impact on reservoir production performance, it is equally important to take advantage of explicit fracture modeling methods with DFN technology to describe the heterogeneity of shale reservoirs and the complexity of fracture networks. The combination of proper stimulation and simulation tools can help obtain more reliable production forecasts and develop fields more effectively.

CHAPTER V

DEVELOPMENT OF THE STOCHASTIC DFN: A HFTS FIELD CASE

This chapter presents an overview of Wolfcamp HFTS project and gathers important field information that can aid in reservoir and fracture system characterization, based on which, a guideline is proposed to integrate varieties of field data as modeling and simulation inputs. A stage-scale stochastic DFN model is developed and then validated by history matching with actual pressure-production data.

HFTS Project Overview

In 2015, Wolfcamp Hydraulic Fracturing Test Site (HFTS) in west Texas was put into operation. A three-dimensional view of the 11 well trajectories in this project is shown in **Fig.23**. Thanks to multiple operators' efforts, a large amount of subsurface information was acquired from this site, giving us a rare and direct insight of underground fracture populations.

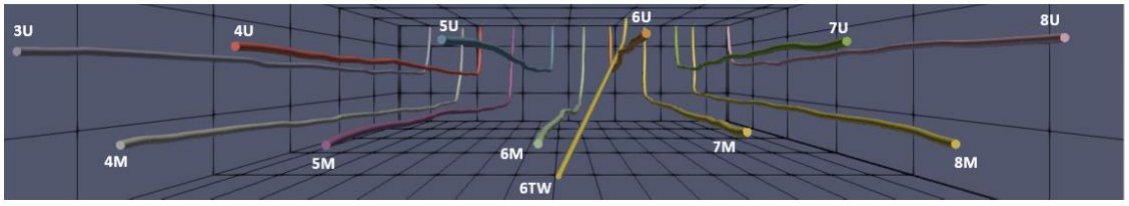

Figure 23 Well trajectories of 11 horizontal wells and 1 slant well in the HFTS. Reprinted from Wood et al. (2018).

Some of the important collected data were concluded as follow:

- Core data. Six continuous and intact cores with a total length of 596 ft were extracted along the slant well, SCW. Core 1 to 4 (~441 ft long in total) captured the stimulated reservoir volume in the vicinity of the 6U well and core 5 to 6 (~160 ft long in total) captured the SRV near the 6M well. Over 700 fractures including hydraulic fractures, two sets of calcite-filled natural fractures in opening mode, drilling induced and core handling fractures were identified from these cores. One-dimensional scanline fracture density, orientation, kinematic aperture and proppant distribution therein were documented and analyzed (Gale et al. 2018; Gale et al. 2019; Maity et al. 2018).
- Open-hole and cased-hole petrophysical, production and image logs were recorded for multiple wells. Amongst them, the spatial distribution of fractures indicated by totally 2400-ft-long image logs along the SCW and two producing horizontals, 6U and 6M, was compared with the fracture location indicated in the core. However, the quality of these three logs were not ideal as they captured fewer fractures than those recorded by cores (Gale et al. 2019). Despite that, other log data were incorporated into a 3D geocellular reservoir model (Wicker et al. 2016) and were used to provide formation petrophysical properties as indicators of fracture density prediction models (Campbell et al. 2018).
- Microseismic data. An extensive microseismic survey with dual-sensor array (vertical and horizontal) over 400 stages of the entire HFTS field

were conducted. The generated microseismic heat maps indicated the event density and dimension of stimulated reservoir volume. According to the microseismic data, the 11 horizontal wells had an average fracture half-length of 830 ft and an average fracture height around 800 ft (Trowbridge et al. 2017; Stegent and Candler 2018; Maity 2018).

- Pre- and post-treatment seismic data. During the early stage of the development of the Midland Basin Wolfcamp play, the Laredo Petroleum company utilized seismic attributes to create a 3D geo-cellular earth model to determine 'high-potential' hydrocarbon intervals and well location (Wicker et al. 2016). Later on, during the stimulation treatment, low-frequency seismic events were recorded as supplementary information of microseismic data, aiding in the detection of tensile failure of hydraulic fractures and deformation in clay-rich ductile shale (Kumar et al. 2018a).
- Well interference data. Bottom hole gauges installed in multiple wells could continuously record the pressure response of monitor wells induced by adjacent source wells during well testing. There were two well tests in the HFTS program, two pressure buildup operations after approximately 7 and 18 months of production. Initially, it was discovered from the interference data that the hydraulic communication among the wells in the Upper Wolfkamp formation was stronger than that in the Middle Wolfkamp formation. Later on, this relationship was reversed due to

different fracture closure rates in these two intervals (Kumar et al. 2018b; Li et al. 2019).

- Tracer recovery data. In addition to pressure interference tests, three types of tracers were also employed to detect the vertical and horizontal communication between wells, including radioactive proppant tracers, water-based and oil-based chemical tracers. The spectral gamma ray log was run to detect the coverage of radioactive proppant tracers and hydraulic cluster efficiency along the wellbore. Surface flowback sampling in many wells captured the concentration of oil/water chemical tracers in the produced fluid. Tracer recovery and pressure interference data were in agreement with each other that wells in the HFTS have complex and high degree of fluid exchange, in which the water communication across the zone was way stronger than oil and proppant transportation (Wood et al. 2018).
- PVT data of sampled reservoir fluids. Produced oil samples were collected in every horizontal well and their PVT properties were assessed through lab experiments. The results were made publicly available through an online database called NETL's Energy Data eXchange, which belongs to the National Energy Technology Laboratory. This study referred to the PVT data of the 6U well. The black oil model has been listed in **Table 6** and was displayed in a more straightforward way in **Fig.24** and **25** here. A

reservoir temperature of 156°F and a reservoir pressure of 4087.7 psia were determined from laboratory PVT analysis.

- Production and BHP data. For all 11 wells, oil/gas/water production rates are available on DrillingInfo, a comprehensive information resource platform and the bottom-hole flowing pressure (BHP) of the first 500 days are available on NETL's Energy Data eXchange. Again, take the 6U well as an example, its daily production and BHP data are summarized in **Fig.26**.
- Other data. Other field information such as Micro Diagnostic Formation Injection Tests (DFIT) that provides reference value of minimum horizontal stress, outcrop mapping, Distributed Acoustic and Temperature Sensing (DAS/DTS) were included in the data acquisition program (Ciezobka et al. 2018).

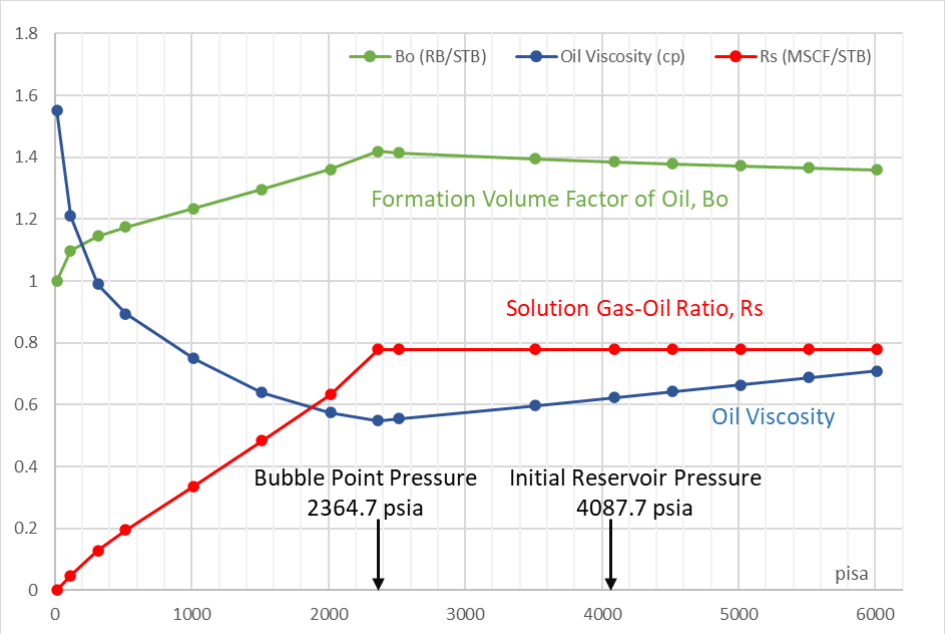

Figure 24 Formation volume factor of oil, oil viscosity and solution gas-oil ratio data of the fluid sample from the 6U well.

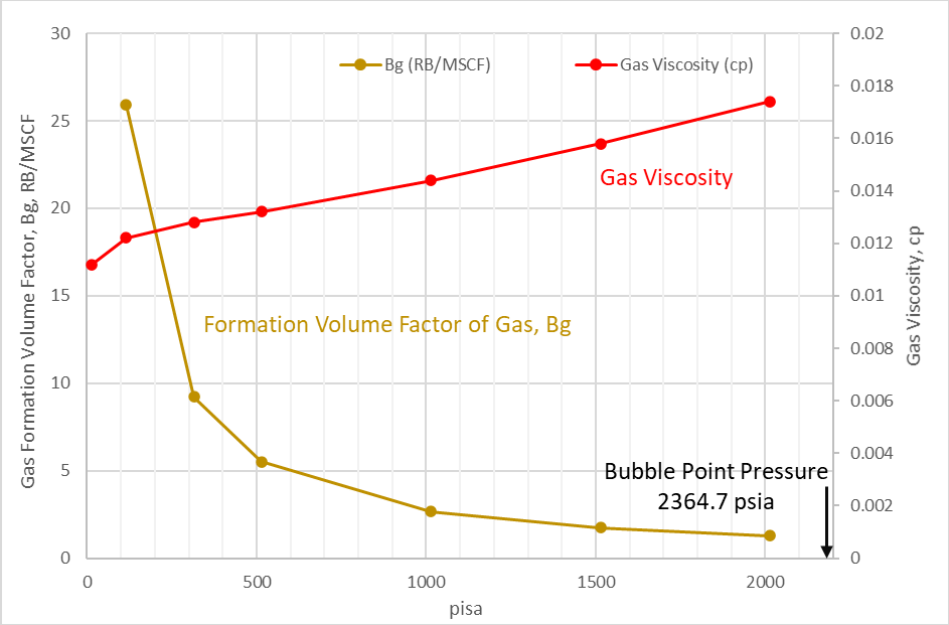

Figure 25 Formation volume factor of gas and gas viscosity of the fluid sample from the 6U well.

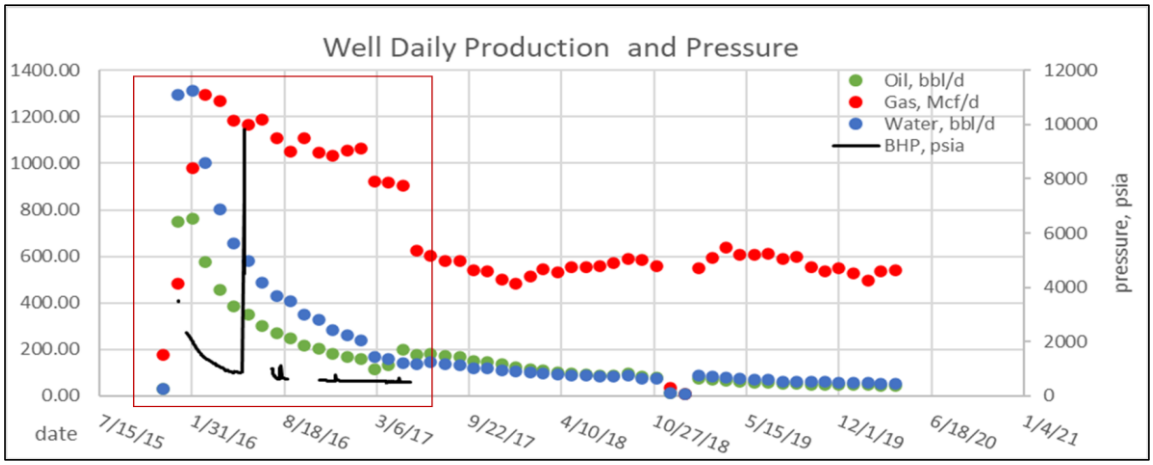

Figure 26 Daily productions rates (source: DrilingInfo) and BHP historical data (source: NETL's Energy Data eXchange) of the 6U well.

On the basis of the data collected above, several studies have attempted to characterize the fracture system and extrapolate it to a field scale. Their methods could be divided into two categories: deterministic geology-based method and implicit flow-based method.

The first category developed models with direct field data to represent the spatial distribution of fractures. For example, as mentioned before, the Laredo company incorporated seismic data with other important geophysical and geomechanical properties into an earth model to predict short-term cumulative oil production (Wicker et al. 2016). In addition, Campbell et al. (2018) correlated log suite information with realistic fractures observed from the cores along the slant well to determine controlling variables for fracture density, such as gamma ray and shallow resistivity. Then, analytical models were built to predict natural and hydraulic fracture density across the HFTS play based on reservoir petrophysical and geomechanical properties indicated by logs. Another stage-scale DFN

was developed by Shrivastava et al. (2018) in a stochastic manner. Natural fracture populations were generated by their in-house simulator, in which fracture density and orientation were determined directly based upon the cores. The fracture lengths were generated with a statistical power-law distribution as probability density and calibrated with a 'synthetic coring procedure'.

Alternatively, microseismic events were believed to provide estimates of hydraulic fracture density around a stimulated well. Wicker et al. (2018) compared the microseismic event density map with cores in the same interval, results of which displayed high consistency of hydraulic fracture locations. However, Maity et al. (2018) found that the vertical and lateral extensions of induced hydraulic fractures indicated by microseismic events (the average height of the 11 HFTS wells is approximately 800 feet and the lateral half-length is approximately 85 feet) far exceeded the propped fracture extensions indicated by proppant distribution (approximately 30 feet in height and 85 feet in lateral half-length for wells in the Upper Wolfcamp formation), making it difficult for modeling and simulation studies to determine the effective fracture geometry. It was concluded that microseismic data did provide valuable information about the stimulated reservoir volume (SRV). But when it came to precise fracture geometry determination, they needed to be integrated with other field information to ensure the accuracy.

Except direct descriptions of the fracture system, fluid flow behaviors documented for the HFTS such as pressure interference, rate transient analysis and tracer recovery were regarded as implicit indications of fracture network connectivity and conductivity. For instance, Kumar et al. (2018b) proposed a conceptual fracture overlapping model in

attempt to match the historical pressure response recorded between a source well and a monitoring well. The reservoir permeability was determined as 180 nD and the extension of fracture overlapping between wells was around 12 ft.

The well-rounded data acquisition program in the HFTS project has provided the industry with plenty of valuable data. In light of the studies demonstrated above, the next section of this chapter proposes a methodology to integrate available field data as much as possible to characterize the spatial distribution of natural fractures over the field. We also build a stochastic DFN model and calibrate it with actual production rates.

Stochastic DFN Model Initialization

After all public field information is gathered, this study narrows the target from the entire field down to the 6U well which possesses the most sufficient fracture evidence of high quality from 4 continuous slant cores to reduce the computation cost, as explained in Chapter 2. The overall workflow of reservoir model development starts with field data integration, as summarized in **Fig.27**. As the right-hand side of the diagram indicates, two categories of inputs are needed for DFN modeling: geometry-related and simulation-related data. We will explain them one by one.

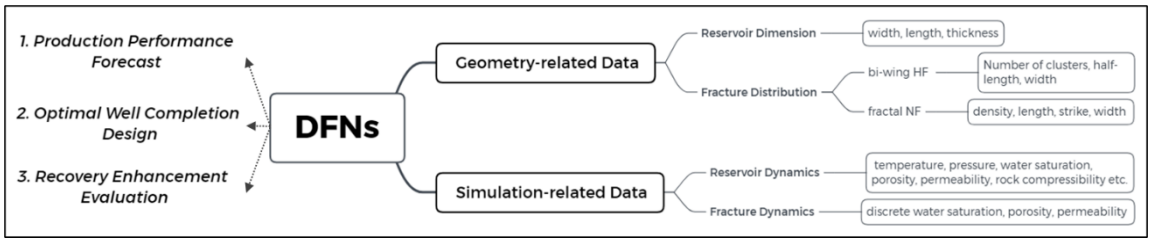

Figure 27 Guideline for field data integration.

Reservoir Dimension

The model width *W*, length *L* and thickness *H* can be determined by either the microseismic-constrained stimulated reservoir volume (SRV) or a clearly defined no-flow boundary. In the HFTS project, the spacing between a horizontal well and its nearest neighboring wells in the same formation is 660 ft. The lateral length of the 11 wells is approximately 10, 000 ft, which is too big for a DFN model that allows intensive natural fractures to be taken into account. The explicit and flexible representation of geological features in DFN models inevitably comes along with great computation costs during discretization and simulation processes. Therefore, we decide to focus on one stage of the 6U well and believe it can be a representative element of the whole well. It was completed with a design of 3-cluster 90 ft spacing, so the dimension of our reservoir model is 660 feet width by 270 feet length. The model height is determined as 150 ft.

Fracture Distribution

For stochastic DFN models, natural fractures are usually generated with certain probability distribution frequencies (PDFs) since their geometries are observed to exhibit similar features at increasing scales in many natural fields. Researchers collect fracture

length, density, aperture, height and orientation distributions from limited but representative volumes in the field and analyze the collected data in a statistical way. Then, these distributions can be extrapolated to any desired model scale. In this study, a two-dimensional fracture generator is developed based on Kim and Schechter's work (2009), to populate stochastic natural fractures over the reservoir model domain. This generator adopts the multiplicative cascade method to reproduce fracture clustering nature rather than the uniformly random generation of fracture centers.

Chapter 1 has introduced a few commonly used PDFs. In the HFTS field, two sets of calcite-filled natural fractures in opening mode have been discovered and interpreted through extracted cores and FMI image log (Gate et al. 2018; Gate et al. 2019). They are abundant and sub-vertical so that the natural fracture strike and aperture distribution are directly determined from these data. As **Fig.28** shows, the primary set strikes NE-SW and the second set strikes WNW-ESE. The fracture kinematic apertures are summarized in **Fig.29**, where set 1 follows a negative-exponential function and set 2 does not seem to follow a specific distribution strictly. Occurrences of other types of natural fractures are minor and thus not included in this model.

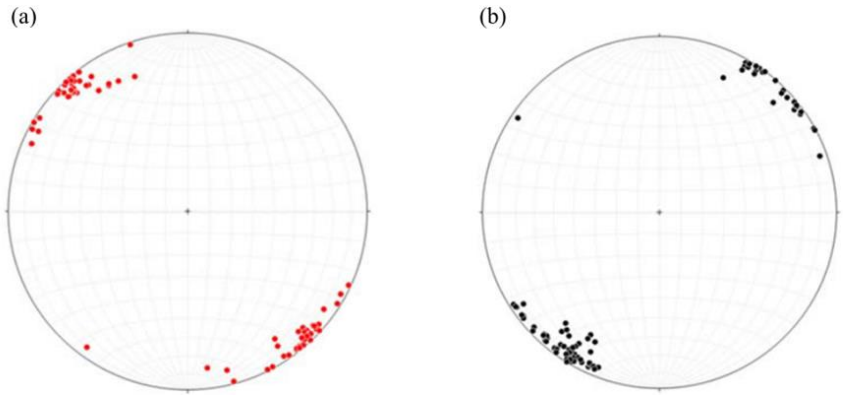

Figure 28 Lower-hemisphere stereograms of poles to 2 sets of natural factures interpreted based on core data. a) set 1; b) set 2. Reprinted from Gale et al. (2018).

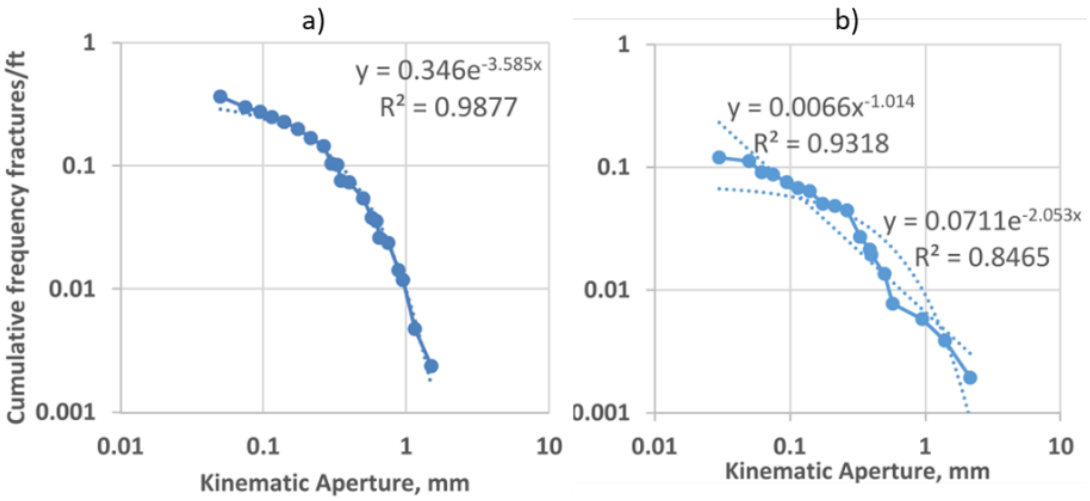

Figure 29 Cumulative frequencies of fracture kinematic aperture distribution. a) set 1; b) set 2. Reprinted from Gale et al. (2019).

At the same time, the determination of fracture density and length in the model is more challenging. One-dimensional scanline measurement of fracture density along the SCW is inadequate to guarantee a precise description of fracture spatial distribution. Similarly, the size of cores makes it impossible to provide valuable information for intact fracture length distribution. As a result, this study adopts the first-order model to correlate

fracture center distribution and fracture length distribution. Recall the first-order model in Chapter 1 as:

$$N(L) = \frac{\alpha L^{D_c}}{D_l}\left({l_{min}}^{-D_l} - {l_{max}}^{-D_l}\right) \qquad eq.2(b)$$

In this case, the effective sampling domain L , 128.7 m, is calculated from the root of reservoir model width 660 ft and length 270 ft. The constant term α refers to an areal density of 0.45 fractures/m^2 within a 100m-by-100m reservoir domain, which is validated by a synthetic coring process in the study of Shrivastava et al. (2018). l_{min} is defined as 0.02 L. It is found in most fields that the fractal dimension of fracture length D_l varies within a range of [0.7, 1.8] and the fracture dimension of fracture center distribution D_c varies within a range of [1.5, 2] (Bonnet el al. 2001). A relationship, $D_c \geq D_l$, is also very common in natural fracture systems (Darcel el al. 2003). In this regard, a simple sensitivity analysis is conducted to determine the value of D_c and D_l.

With the abovementioned fracture information as inputs, our in-house fracture generator develops six natural fracture maps with different D_c and D_l. All of the cases are shown in Appendix A. **Fig.30** displays one of them as an example case, whose $D_c = 1.85$ and $D_l = 1.8$. From these cases, we do observe that the degree of fracture clustering and the relative proportion of long and short fractures are influenced by D_c and D_l. However, when we try the same preliminary production test on all cases, similar production trends are observed and the minor difference between them can be eliminated by adjusting flow-related simulation parameters such as fracture permeability. One possible explanation is that when the abundance of natural fractures reaches a certain degree, when fracture strike,

aperture distributions are fixed and when fracture centers, lengths are constrained by the same statistical model, large-scale reservoir production is no longer sensitive to specific fracture center locations and the ratio of long to short fractures. An alternative explanation is that accurate descriptions of the fracture network geometry and of fracture conductive properties are equally important for successful modeling and simulation. Multiple combinations of different simulation parameters may result in the same production behavior. In this regard, out of the six cases, the case with the least number of fractures in **Fig.30** is selected as the basis for further simulation to save some computation time.

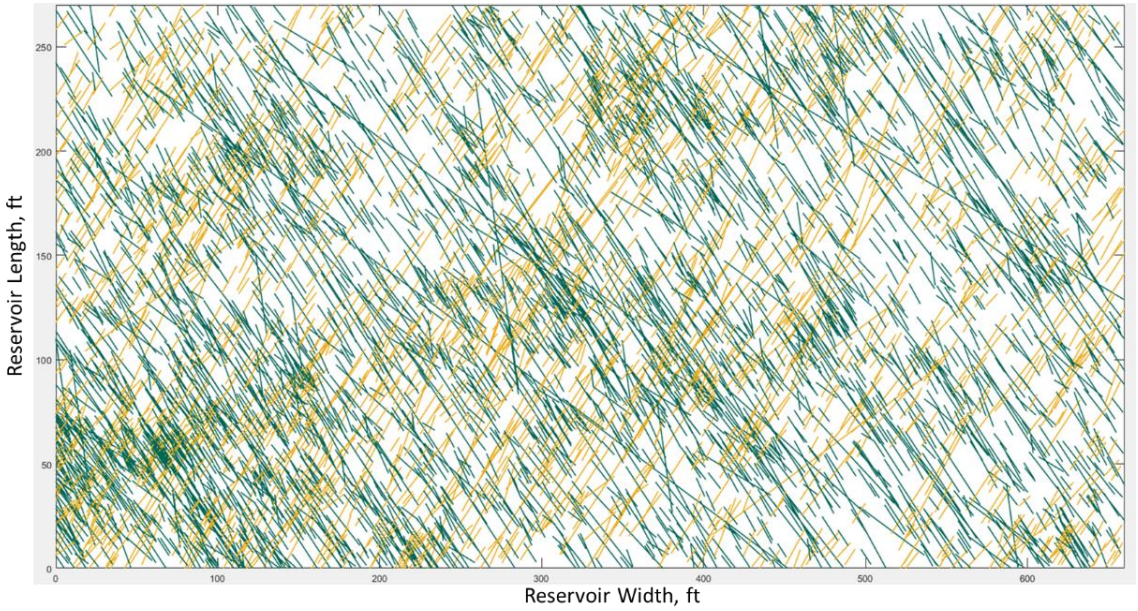

Figure 30 Stochastic fractures generated with D_c=1.85 and D_l=1.8. The primary set is represented by the green lines and the second set is plotted by yellow lines.

As for hydraulic fractures, the 6U well was completed with the design of 37 stages in total and 3 clusters spaced 90 ft apart in one stage. In our model, each cluster is assumed

to form a single hydraulic fracture that is orthogonal to the well trajectory. The definition of hydraulic fracture half-length in modeling has been controversial. While some researchers claim that microseismic events are a good indicator of fracture half length (Trowbridge et al. 2017), others find them over optimistic (Bazan et al. 2010; Edwards et al. 2011). According to Friedrich and Milliken's (2013) analysis of early microseismic data for the Upper Wolfcamp formation, only about 25% of microseismicity-indicated SRV is conducive to production. In addition to that the fracture half-length of well 6U is constrained to around 1,000 ft by microseismic density maps (Stegent and Candler 2018), the HF half-length in our model is defined as $1000 \times 25\% = 250\ ft$.

As previously discussed, the HF-NF interaction and hydraulic propagation processes are not main objectives of this study, thus we simply overlay natural fractures and hydraulic fractures in the same model to constitute a stage-scale DFN, as **Fig.31** shows. We believe only natural fractures that are well connected to hydraulic clusters have the best chance to be activated and propped, and consequently make a major contribution to production. So we discard isolated and small-scale fractures (<5 ft long) that have negligible influence on flow. Or in other words, their contribution is incorporated into effective matrix permeability enhancement (Bourbiaux et al. 2005) that will be tuned later.

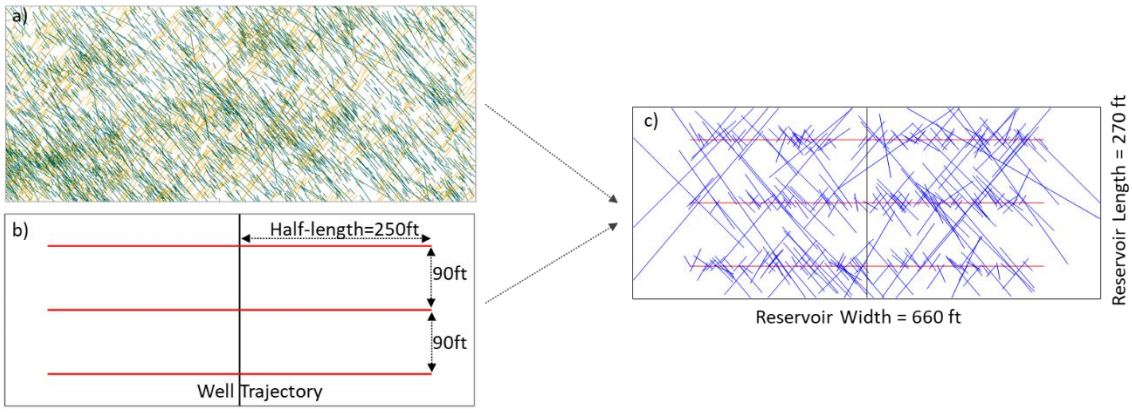

Figure 31 Incorporation of natural and hydraulic fractures into a 660'-by-270' model. a) two sets of stochastic natural fractures; b) one stage of three hydraulic fractures, represented by red straight lines; c) connected natural fractures in blue and hydraulic fractures in red.

Once the 2D model is developed, our software 'iUnconventional' discretizes it with unstructured PEBI cells. As **Fig.32** displays, fractures are refined by tiny cells highly conforming to their geometric shapes. The size of cells gradually increases as they move far away from fractures.

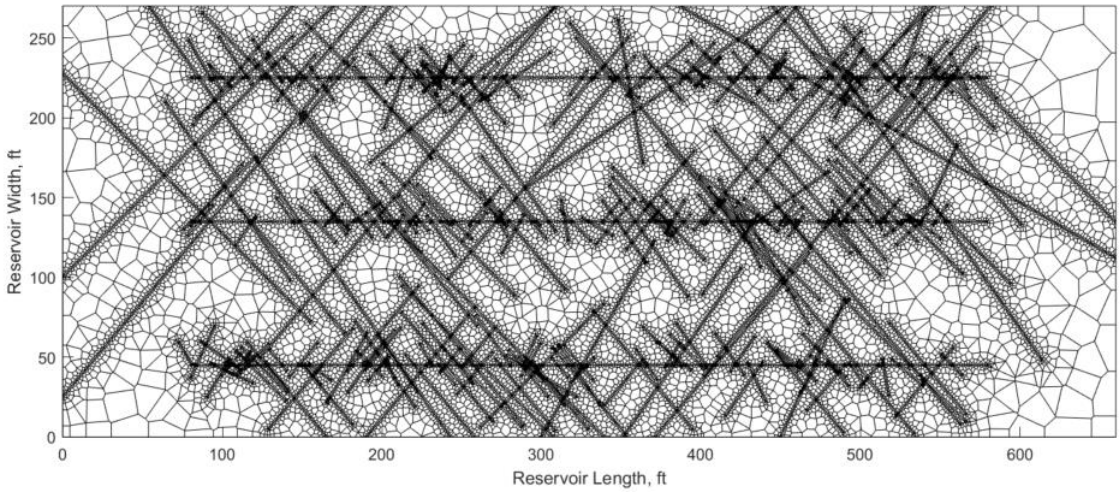

Figure 32 2D fracture model meshed with unstructured PEBI cells.

Reservoir Dynamics

To fully describe reservoir flowability, several types of parameters need to be defined in the simulation: 1) parameters that can be directly measured on site or analyzed in the laboratory, such as initial reservoir temperature (which remains constant during production), initial reservoir pressure, fluid PVT and relative permeability properties; 2) parameters that need to be averaged as single representative values for simulation purpose, but usually standard logging suites only provide estimates of their ranges of variation along the measured depth, such as initial water saturation, matrix porosity, matrix permeability and so forth; 3) parameters missing from the field. Except parameters involved in the first two types, the assignments of other flow-related parameters may not be able to take advantage of field information. Reference values from adjacent reservoirs, literatures or online database are desired.

Fracture dynamics

It is almost impossible to measure the permeability, porosity and initial water saturation of both natural and hydraulic fractures. Typically, initial water saturation inside the fracture is likely to be higher than it in the matrix due to stimulation fluid residues. Natural fracture permeability in shale reservoirs may be several orders of magnitude higher than matrix permeability and the conductivity of hydraulic fractures may reach infinity. When the fracture aperture is known, fracture permeability can be determined via Cubic Law. These values will be initialized with reference values first and then adjusted later.

So far, this proposed workflow has completed the DFN model initialization process. **Table 11** summarizes initial simulation settings. It is noteworthy that there are still some parameters that remain uncertain. It is essential to couple the geologically represented model with dynamic flow data to determine their values. In the context, a sensitive study is conducted in the next section to see their individual impacts on reservoir performance.

Table 11 Simulation Parameters of HFTS DFN Model Initialization.

Determinate Inputs		**Uncertain Inputs**	
Properties	**Value**	**Properties**	**Value**
Reservoir Dimension, ft	660×270×150	**Matrix Permeability, mD**	0.0004
Datum Depth, ft	7700	**Matrix Porosity**	0.06
Reservoir Temperature, degF	156	**Initial Water Saturation**	0.5
Initial Pressure, psia	4087.7	**Rock Compressibility, 1/psi**	3.00E-05
Saturation Pressure, psi	2364.7	**Fracture Compressibility, 1/psi**	3.00E-05
HF Half-length, ft	250	**NF Porosity**	0.12
HF Spacing, ft	90	**NF Permeability**	2.76
HF Permeability	Cubic Law	**HF Porosity**	0.3
Fluid Model	HFTS Black Oil	**HF Aperture, ft**	0.03

The generated two-dimensional DFN in **Fig.32** is extruded to 2.5D by specifying a reservoir thickness 150 ft. Next, the fracture model and a calculated connection list are exported to Nexus to run a trial reservoir depletion test, resulting in a pressure distribution map as **Fig.33**. This map is generated by exporting the simulation result back to our software 'iUnconventional'. The post visualization module is able to generate pressure/saturation/transmissibility distribution maps for DFN.

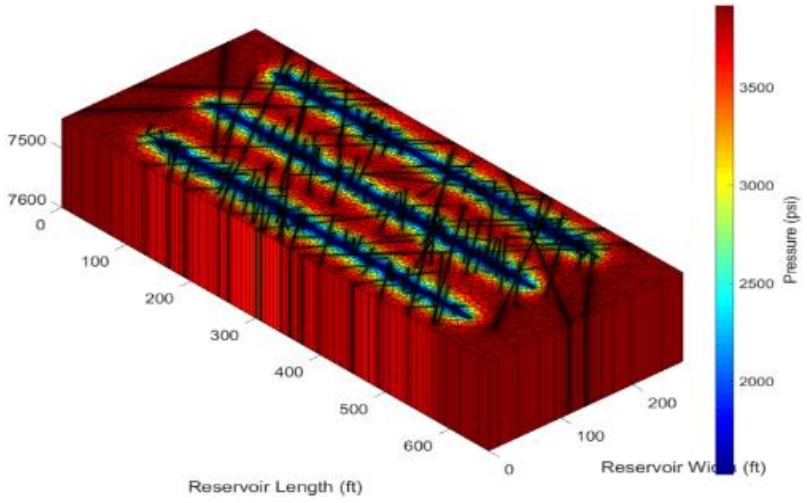

Figure 33 Pressure distribution map after a primary depletion test.

The implementation of such a guideline makes the best of available field observations and measurements at multiple scales to build a stochastic DFN model. Every formation must be evaluated on its own merits but this workflow is also applicable for the modeling and simulation of other unconventional reservoirs. Except the first-order model, other NF-related PDFs provided in Chapter 1 can also be utilized in fracture generation.

Sensitivity Analysis and History Match

From the last two sections we find out that even with the most advanced data acquisition program in the HFTS, to build a reliable reservoir model, there are still a lot of parameters left unknown from direct sampling. The objective of this section is to understand the impacts of these uncertain parameters on reservoir performance and determine representative values for them. To do so, **Table 12** lists 9 uncertain parameters as independent variables. Daily production rates, BHP data of the 6U well in **Fig.34** are listed as objective functions of a sensitivity analysis. Note that we assume an equal production contribution of every stage along the 6U well, so the total well rates are divided by 36, the number of active stages of the 6U well, to represent the production of a one-stage model.

Table 12 Sensitivity Analysis for 9 Uncertain Variables.

	Variable Settings			Objective Function Trends			
	Parameters	**Initial Value**	**Variation Range**	**Oil Rate**	**Gas Rate**	**Water Rate**	**BHP**
Reservoir Properties	**Rock Compressibility, 1/psi**	3.00E-05	[3.00E-06, 3.00E-04]	↑	greatly↓	↓	↑
	Matrix Permeability, mD	0.0004	[0.00012, 0.0008]	slightly↓	↓	slightly↑	↑
	Matrix Porosity	0.06	[0.04, 0.12]	↓	↓	↑	↑
	Swi of Matrix	0.5	[0.3, 0.65]	greatly↓	greatly↓	greatly↑	↑
Fracture Properties	**HF Width, ft**	0.03	[0.01, 0.03]	slightly↑	x	slightly↓	↑
	Fracture Compressibility, 1/psi	3.00E-05	[3.00E-5, 5.00E-6]	x	slightly↑	x	slightly↓
	NF Permeability, mD	2.76	[0.001, 10]	x	↓	x	↑
	NF Porosity	0.15	[0.04, 0.15]	x	x	x	x
	HF Porosity	0.15	[0.1, 0.3]	x	x	x	x

The 9 independent variables are: rock compressibility, matrix permeability, matrix porosity, initial water saturation of matrix, hydraulic fracture width (accordingly HF permeability is calculated based on the Cubic Law), fracture compressibility, natural fracture permeability (we suspect Cubic Law may be too optimistic for NF permeability due to their roughness), porosity of natural and hydraulic fractures. **Table 12** summarizes the initial setting, variation range and simulated objective function trends for each of them. The one-factor-at-a-time (OFAT) method is implemented for the experiment design. For instance, according to references (Stegent and Candler 2018; Kumar et al. 2018), Upper

Wolfcamp formation has a permeability ranging from 120 to 800 nD. Within this range, by increasing matrix permeability (k_m) and keeping other variables at the initial settings, we can observe a decline trend in gas production, slight changes in oil and water production, and an increase in BHP. We conduct similar simulation experiments for the other 8 variables. The terms 'slightly' or 'greatly' describe the variation extent of objective functions. The cross sign denotes that the variable has minor impact on that specific objective function.

A tornado chart is also created in **Fig.34** to evaluate the relative impact of the 9 variables on BHP. Taking reservoir permeability as an example again, the simulation performed with its lower limit, 0.00012 mD, yields a negative deviation of 726 psi from the actual BHP data. When reservoir permeability is set to 0.0008 mD, the simulated BHP is 1640 psi higher than the actual BHP. Other parameters can be analyzed in the same way. Although the degree of BHP variation is subject to many other variables, this tornado chart and the objective function trends obtained above can be utilized as guidelines for a manual history matching process.

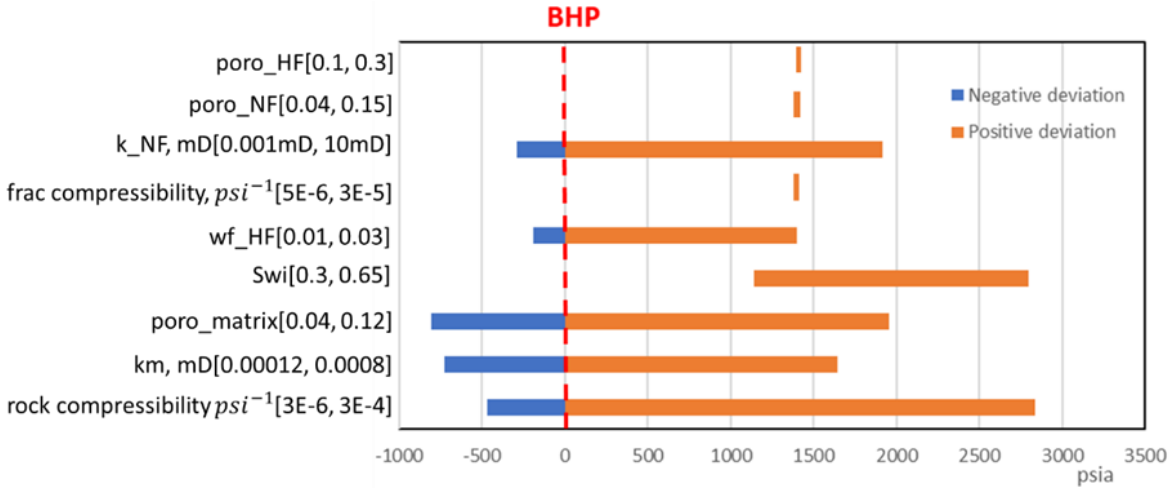

Figure 34 Tornado chart of BHP sensitivity analysis.

As can be discovered in **Fig.34**, hydraulic fracture porosity, natural fracture porosity and fracture compressibility rank as the least significant constrolling factors of BHP. Thus, they are kept the same as their initial settings. The rest 6 variables are adjusted to match the historical production and BHP data. Since assisted history matching of discrete fracture models meshed with unstructured cells has not been available on commercial simulators yet, manual history match is accomplished by numerous attempts of trial and error in this study. **Fig.35** demonstrates the eventual BHP match, cumulative production match for oil, gas and water.

At the very start of this chapter, we mentioned that two well tests were performed on the HFTS wells after approximately 7 and 18 months of production. Unfortunately, detailed information of well tests is private so we cannot simulate these processes. As far as the first 200 days are concerned, the quality of our history match is convincing.

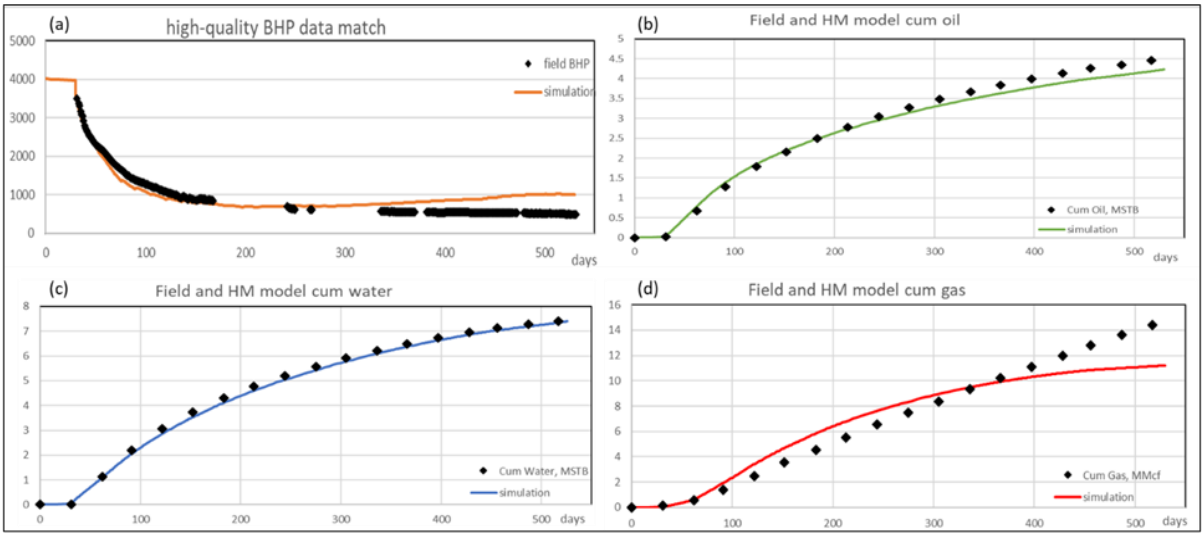

Figure 35 Comparison between historical field data indicated by black dots and simulation data represented by colorful curves. (a) BHP match; (b) cumulative oil rate match; (c) cumulative water rate match; (d) cumulative gas rate match.

Table 13 lists the initial values of six adjusted variables and the updated values after historical matching. As it is known, a history match might be realized by multiple combinations of parameters. Updated values in **Table 13** might be one of them. But we believe through this study, we understand this reservoir to a certain degree.

Table 13 Initial and Updated Values of 6 Variables.

Parameters	Initial Value	Updated Value
Rock Compressibility, 1/psi	3.00E-05	3.00E-05
Matrix Permeability, mD	0.0004	0.0005
Matrix Porosity	0.06	0.063
Swi of Matrix	0.5	0.56
HF Width, ft	0.03	0.02
NF Permeability, mD	2.76	2.3

Static Surfactant Flooding Test

Next, upon the validated model, a simple static surfactant flooding test is performed. Since the HFTS has not practiced surfactant techniques in the field yet, data presented in this section might not represent reality but the EOR application of DFNs is demonstrated.

Surfactant, as one of the main enhanced oil recovery (EOR) technologies for unconventional play exploitation, has become the research hotspot in recent years due to its characteristics of low cost, ready availability, low risk and high reward. Usually, surfactants are injected with the stimulation flood during hydraulic fracturing. We assume that after surfactant flooding, surfactants penetrate into matrix from fractures and manage to change the wettability of this surfactant-invaded zone. Two sets of relative permeability curves (k_r) and capillary pressure (P_c) curves are displayed in **Fig.36**, with one representing an oil-wet case before surfactant flooding and one representing a water-wet case after surfactant flooding. These data are referred from a lab-scale history matching study of the Wolfcamp B sample (Zhang 2020).

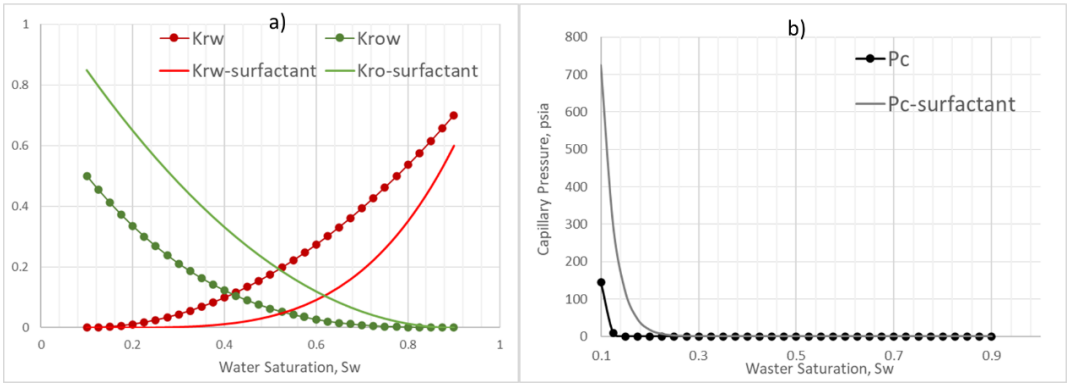

Figure 36 Relative permeability (a) and capillary pressure (b) profiles before and after surfactant flooding. Data referred from Zhang (2020).

Based on the model developed from the previous section, three simulation cases are performed to depict 3 scenarios: no surfactant, surfactant penetrating matrix for 1 ft, and surfactant penetrating matrix for 2 ft. The 'iUnconventional' is able to assign different matrix zones with different saturation and relative permeability properties for DFN models. For the surfactant invaded zone, the water-wet relative permeability and capillary pressure profiles in **Fig.36** are applied while for the rest matrix backgrounds, oil-wet curves are applied in the simulation. The simulated production results are shown in **Fig.37**.

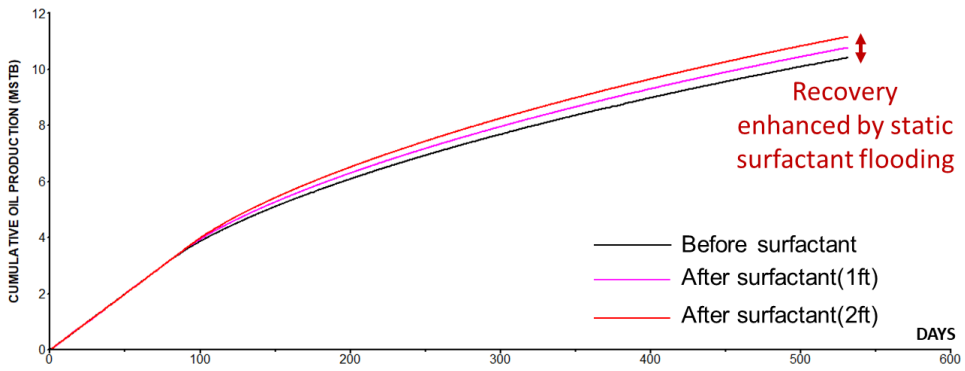

Figure 37 Cumulative production results of cases without surfactant, with surfactant entering matrix for 1 ft and with surfactant entering matrix for 2 ft, respectively.

Using the k_r and P_c profiles in **Fig.36**, if the surfactant enters matrix for 1 ft, the recovery factor would increase by 0.17 % and if the surfactant enters matrix for 2 ft, the recovery factor would increase by 0.37 % after 500-day production. The default penetration distance of the surfactant is conservative, which leads to tiny recovery increments. But we do observe that the recovery is enhanced by the surfactant simulation and expect its potential in the field application. Further research about the surfactant

functioning mechanism and upscaling lab-derived relative permeability curves to field-scale simulation in unconventional reservoirs are required.

CHAPTER VI

CONCLUSIONS

Unlike conventional reservoirs, substantial permeability contrast between the fracture and the matrix in unconventional reservoirs makes the conductive fracture network dominate the fluid flow and hydrocarbon production. From this perspective, explicit representation of fracture systems benefiting from our powerful DFN techniques is of critical importance for unconventional plays. Through this study, two main topics are investigated: modeling the spatial distribution of natural fractures and simulating fractured reservoir models.

In order to represent natural fractures, two types of models are generated, including the geologically represented DFN and the stochastically generated DFN. Both models have pros and cons. The first type of DFN can reproduce the exact geological features of fractures in the field. However, the size of such a model is inevitably limited to the sampling scale, for example, the dimension of collected outcrops. The other stochastic model is scale-independent. But even with the same set of statistical parameters, multiple different realizations of fracture distribution could be generated. Flow-related data are essential for the calibration of these models.

Less attention was paid to hydraulic fractures in this study. The typical bi-wing model is still used to represent multi-stage hydraulic clusters. But in the HFTS, the abundance of hydraulic fractures has been discovered to be greater than that of natural fractures. As more and more field evidences reveal that hydraulic fractures propagate in

the form of complex triplets/doublets/swarms, their characterization would become an increasingly important factor in building reliable reservoir models. The complex interaction between hydraulic fractures and pre-existing natural fractures also needs to be investigated in future work.

Besides, the suggestion for designing non-uniform stimulation treatment proposed by Chapter 4 needs to be further tested with different reservoir settings. Incorporating natural fractures in the model and introducing more variation scenarios such as non-uniform fracture spacing would make the study more interesting and more convincing.

The other main topic of this study, simulation of developed DFN models, has helped us understand how fracture features such as NF aperture and permeability influence the reservoir production. Reservoir simulation also helps us figure out which parameter has prior impact on and which parameter ranks as the least important controlling variable to the output objectives. In return, a successful history matching simulation has validated the DFN model developed with many variables indetermined from direct field observations, making it possible to further forecast the production, optimize current field development strategies or select a proper EOR technique.

The fluid models used in our simulation were black oil models. In the future, compositional simulation, EOR simulation and other advanced simulations might assist DFN technique to gain more attention. The dimension of DFN models is limited to the stage scale in this study to avoid great computation costs associated with fracture generation and unstructured girding process. Upscaling the DFN to field-scale modeling and simulation can be a goal of further research.

At last, some of key takeaways from this study are concluded as below:

1) The in-house software 'iUnconventional' with functions of fracture generation, unstructured meshing and post visualization is powerful and reliable.
2) Hydrocarbon production is positively correlated with NF conductivity but less sensitive to HF conductivity as it has reached infinite conductivity.
3) The assignment of non-uniform aperture and permeability is good for small-scale DFN models, but non-uniform fracture aperture can be represented by a properly defined constant aperture in large-scale modeling for simulation simplicity.
4) Non-uniform hydraulic fracturing patterns generally perform better than the uniform stimulation design at the same stimulation cost, in terms of cumulative oil production. Clustered fracturing should be avoided as it leaves large intact volumes of matrix undrained. Creating a large SRV boundary is conducive to hydrocarbon production.
5) Cluster productivity greatly depends on the dimension of induced hydraulic fractures, especially as the contrast between matrix and fracture permeability increases.
6) The stochastic method of DFN generation is able to integrate multi-scale field data.
7) Realistic BHP, oil, gas and water production data from the HFTS project are matched with the developed stochastic DFN. The sensitivity analysis indicates

that important controlling variables of reservoir performance are rock compressibility, rock and natural fractures permeability.

8) Static surfactant EOR is tested on the stochastic DFN by assigning a more favorable wettability to regions near fractures. The recovery of a 500-day depletion increases by up to 0.37%.

REFERENCES

1. Kim, T. H. 2007. Fracture characterization and estimation of fracture porosity of naturally fractured reservoirs with no matrix porosity using stochastic fractal models. Dissertation. Texas A&M University, College Station, TX.

2. Sun, J. 2016. Characterization and Simulation of Discrete Fracture Networks in Unconventional Shale Reservoirs. Dissertation. Texas A&M University, College Station, TX.

3. Niu, G. 2019. Characterization of Fractured Reservoir and Simulation of EOR Techniques. Dissertation. Texas A&M University, College Station, TX.

4. EIA (US Energy Information Administration). 2020. Annual energy outlook, accessed 20 February 2021. https://www.eia.gov/outlooks/aeo/.

5. Narr, W., Schechter, D. S., and Thompson, L. B. 2006. *Naturally Fractured Reservoir Characterization*. Richardson, TX: Society of Petroleum Engineers.

6. Finley, S.J., and J.C. Lorenz. 1989. Characterization and Significance of Natural Fractures in Mesaverde Reservoirs at the Multiwell Experiment Site. Presented at the Low Permeability Reservoirs Symposium, Denver, Colorado, USA, 06 March, SPE-19007-MS. https://doi.org/10.2118/19007-MS.

7. Lorenz, J. C. and Hill, R. E. 1994. Subsurface fracture spacing: Comparison of inferences from slant/horizontal core and vertical core in Mesaverde reservoirs. *SPE Formation Evaluation* **9** (01): 66-72. SPE-21877-PA. https://doi.org/10.2118/21877-PA.

8. Branagan, P. T., Peterson, R. E., Warpinski, N. R. et al. 1996. Characterization of a remotely intersected set of hydraulic fractures: results of intersection well no.1-B, GRI/DOE multi-site project. Paper presented at the Unconventional Resources Technology Conference, Denver, Colorado, USA, 6-9 October. SPE-36452-MS. https://doi.org/10.2118/36452-MS.

9. Hopkins, C. W., Frantz Jr, J. H., Hill, D. G. et al. 1995. Estimating fracture geometry in the naturally fractured Antrim Shale. Paper presented at the Unconventional Resources Technology Conference, Dallas, Texas, USA, 22-25 October. SPE-30483-MS. https://doi.org/10.2118/30483-MS.

10. Montgomery, S. L., Schechter, D. S. and Lorenz, J. 2000. Advanced Reservoir Characterization to Evaluate Carbon Dioxide Flooding, Spraberry Trend, Midland Basin, Texas. AAPG Bulletin **84** (9): 1247-1273.

11. Raterman, K. T., Farrell, H. E., Mora, O. S. et al. 2017. Sampling a Stimulated Rock Volume: An Eagle Ford Example. Paper presented at the Unconventional Resources Technology Conference, Austin, Texas, USA, 24-26 July. URTEC-2670034-MS. https://doi.org/10.15530/URTEC-2017-2670034.

12. Courtier, J., Chandler, K., Gray, D. et al. 2017. Best Practices in Designing and Executing a Comprehensive Hydraulic Fracturing Test Site in the Permian Basin. Paper presented at the Unconventional Resources Technology Conference, Austin, Texas, USA, 24-26 July. URTEC-2697483-MS. https://doi.org/10.15530/URTEC-2017-2697483.

13. Campbell, W., Wicker, J. and Courtier, J. 2018. Natural and Hydraulic Fracture Density Prediction and Identification of Controllers. Paper presented at the Unconventional Resources Technology Conference, Houston, Texas, USA, 23-25 July. URTEC-2934611-MS. https://doi.org/10.15530/URTEC-2018-2934611.

14. Gale, J. F., Elliott, S. J., and Laubach, S. E. 2018. Hydraulic Fractures in Core from Stimulated Reservoirs: Core Fracture Description of HFTS Slant Core, Midland Basin, West Texas. Paper presented at the Unconventional Resources Technology Conference, Houston, Texas, USA, 23-25 July. URTEC-2902624-MS. https://doi.org/10.15530/URTEC-2018-2902624.

15. Warren, J.E., and P.J. Root. 1963. The Behavior of Naturally Fractured Reservoirs. *SPE J.* **3** (03): 245–55. https://doi.org/10.2118/426-PA.

16. Kazemi, H., Merrill Jr, L. S., Porterfield, K. L., et al. 1976. Numerical simulation of water-oil flow in naturally fractured reservoirs. *SPE J.* **16** (06): 317-326. SPE-5719-PA. https://doi.org/10.2118/5719-PA.

17. Pruess, K., and Narasimhan, T. N. 1985. A practical method for modeling fluid and heat flow in fractured porous media. *SPE J.* **25** (1): 14-26. SPE-10509-PA. https://doi.org/10.2118/10509-PA.

18. Beckner, B., Chan, H. M., McDonald, A. E., et al. 1991. Simulating naturally fractured reservoirs using a subdomain method. Paper presented at the SPE Symposium on Reservoir Simulation, Anaheim, California, USA, 17 February. SPE-21241-MS. https://doi.org/10.2118/21241-MS.

19. Fung, L.K. 1991. Simulation of block-to-block processes in naturally fractured reservoirs, *SPE Res Eng* **6** (04): 477–484. SPE-20019-PA. https://doi.org/10.2118/20019-PA.

20. Yan, B., Alfi, M., An, C., et al. 2016. General Multi-Porosity simulation for fractured reservoir modeling. *Journal of Natural Gas Science and Engineering* **33**: 777-791.

21. Doughty, C. 1999. Investigation of Conceptual and Numerical Approaches for Evaluating Moisture, Gas, Chemical, and Heat Transport in Fractured Unsaturated Rock. *Journal of Contaminant Hydrology* **38** (1–3): 69–106.

22. Karimi-Fard, M. and Firoozabadi, A. 2003. Numerical Simulation of Water Injection in Fractured Media Using the Discrete-Fracture Model and the Galerkin Method. *SPEREE **6** (2): 117–126*. SPE-83633-PA.

23. Monteagudo, J. and Firoozabadi, A. 2004. Control-Volume Method for Numerical Simulation of Two-phase Immiscible Flow in Two- and Three-Dimensional Discrete-Fractured Media. *Water resources research **40*** (7).

24. Heinemann, Z. E., Brand, C. W., Munka, M. et al. 1991. Modeling Reservoir Geometry with Irregular Grids. Paper presented at the SPE Symposium on Reservoir Simulation, Houston, Texas, USA, 06 February. SPE-18412-PA. http://dx.doi.org/10.2118/18412-PA.

25. Cipolla, C. L., T. Fitzpatrick, M. J. Williams, et al. 2011. Seismic-to-Simulation for Unconventional Reservoir Development. Paper presented at the SPE Reservoir Characterisation and Simulation Conference and Exhibition, Abu Dhabi, UAE, 09 October. SPE-146876-MS. https://doi.org/10.2118/146876-MS.

26. Fung, Larry S.K., Xiang Y. Ding, and Ali H. Dogru. 2013. An Unstructured Gridding Method for Densely-Spaced Complex Wells in Full-Field Reservoir Simulation. Paper presented at the SPE Reservoir Simulation Symposium, The Woodlands, Texas, USA, February. SPE-163648-MS. https://doi.org/10.2118/163648-MS.

27. Lee, S.H., Lough, M.F., and Jensen, C.L. 2001. Hierarchical modeling of flow in naturally fractured formations with multiple length scales. *Water Resources Research* **37** (3): 443–455.

28. Li, L. and Lee, S.H. 2008. Efficient Field-Scale Simulation of Black Oil in a Naturally Fractured Reservoir through Discrete Fracture Networks and Homogenized Media. *SPE Reservoir Evaluation & Engineering* **11** (04): 750-758. SPE-103901-PA. https://doi.org/10.2118/103901-PA.

29. Moinfar, A., Varavei, A., Sepehrnoori, K. et al. 2014. Development of an Efficient Embedded Discrete Fracture Model for 3d Compositional Reservoir Simulation in Fractured Reservoirs. *SPE J.* **19** (02): 289-303. SPE-154246-PA. https://doi.org/10.2118/154246-PA.

30. Rubin, B. 2007. Simulating gravity drainage and reinfiltration with a subdomain-dual- permeability hybrid fracture model. Paper presented at the SPE Reservoir Simulation Symposium, Houston, TX, February 26-28. SPE-106191-MS. https://doi.org/10.2118/106191-MS.

31. Jiang, J., Younis, R.M. 2016. Hybrid coupled discrete-fracture/matrix and multi-continuum models for unconventional-reservoir simulation. *SPE J.* **21** (03):1–9. SPE-178430-PA. https://doi.org/10.2118/178430-PA.

32. Xu, J., Sun, B. and Chen, B. 2019. A Hybrid Embedded Discrete Fracture Model for Simulating Tight Porous Media with Complex Fracture Systems. *Journal of Petroleum Science and Engineering* **174**: 131–43.

33. Darcel, C., Bour, O., Davy, P. et al. 2003. Connectivity properties of two-dimensional fracture networks with stochastic fractal correlation. *Water resources research*, **39** (10).

34. Lei, Q., Latham, J.P. and Tsang, C.F. 2017. The use of discrete fracture networks for modelling coupled geomechanical and hydrological behaviour of fractured rocks. *Computers and Geotechnics* **85**:151-176.

35. Gale, J. F., Laubach, S. E., Olson, J. E. et al. 2014. Natural fractures in shale: Natural Fractures in Shale: A Review and New Observations. *AAPG bulletin* **98** (11): 2165-2216.

36. Lorenz, John C., and Scott P. Cooper. 2020. *Applied Concepts in Fractured Reservoirs*. John Wiley & Sons.

37. Bourbiaux, B., Basquet, R., Daniel, J. M. et al. 2005. Fractured reservoirs modelling: a review of the challenges and some recent solutions. *First Break*, 23(9), 33-40.

38. Gutierrez, M., and Youn, D. J. 2015. Effects of fracture distribution and length scale on the equivalent continuum elastic compliance of fractured rock masses. *Journal of Rock Mechanics and Geotechnical Engineering* **7** (6): 626-637.

39. Barton, C. A., and Zoback, M. D. 1992. Self-similar distribution and properties of macroscopic fractures at depth in crystalline rock in the Cajon Pass Scientific Drill Hole. *Journal of Geophysical Research: Solid Earth* **97**(B4): 5181-5200.

40. Segall, P., and Pollard, D. D. 1983. Joint formation in granitic rock of the Sierra Nevada. *Geological Society of America Bulletin* **94** (5): 563-575.

41. Heffer, K. J., and T. G. Bevan. 1990. Scaling Relationships in Natural Fractures. Data, Theory, and Application. Paper presented at the European Petroleum Conference, The Hague, Netherlands, 21 October. SPE-20981-MS. https://doi.org/10.2118/20981-MS.

42. Bonnet, E., Bour, O., Odling, N. E. et al. 2001. Scaling of fracture systems in geological media. *Reviews of geophysics* **39** (3): 347-383.

43. Davy, P., Sornette, A., and Sornette, D. 1990. Some consequences of a proposed fractal nature of continental faulting. *Nature* **348** (6296): 56-58.

44. Vicsek, T. 1992. Fractal Growth Phenomena. *World Sci*.

45. Bour, O. and Davy, P. 1999. Clustering and Size Distributions of Fault Patterns: Theory and Measurements. *Geophysical Research Letters **26*** (13): 2001-2004.

46. Bour, O., Davy, P., Darcel, C. et al. 2002. A statistical scaling model for fracture network geometry, with validation on a multiscale mapping of a joint network (Hornelen Basin, Norway). *Journal of Geophysical* Research: Solid Earth **107** (B6): ETG-4.

47. Schertzer, D., and Lovejoy, S. 1987. Physical modeling and analysis of rain and clouds by anisotropic scaling multiplicative processes. *Journal of Geophysical Research: Atmospheres* **92** (D8): 9693-9714.

48. Meakin, P. 1991. Invasion percolation on substrates with correlated disorder. *Physica A: Statistical Mechanics and its Applications* **173** (3): 305-324.

49. Fisher, R. A. 1953. Dispersion on a sphere. *Proceedings of the Royal Society of London. Series A. Mathematical and Physical Sciences* **217** (1130): 295-305.

50. Priest, S. D. 1993. *Discontinuity analysis for rock engineering*. Springer Science & Business Media.

51. Long, J. C., Remer, J. S., Wilson, C. R. et al. 1982. Porous Media Equivalents for Networks of Discontinuous Fractures. *Wat. Resour. Res.* **18** (3): 645-658.

52. Tsang, Y. W. and Tsang, C. F. 1990. Hydrological Characterization of Variable-Aperture Fractures.

53. Tamagawa, T., Matsuura, T., Anraku, T. et al. 2002. Construction of fracture network model using static and dynamic data. Paper presented at the SPE Annual Technical Conference and Exhibition, San Antonio, Texas, 29 September. SPE-77741-MS. https://doi.org/10.2118/77741-MS.

54. Voss, R.F. 1988. Fractals in Nature: From Characterization to Simulation. *The Science of Fractal Images*.

55. Snow, D. T. 1965. A parallel plate model of fractured permeable media. Dissertation. University of California, Berkeley.

56. Sun, J. and Schechter, D. 2015. Optimization-Based Unstructured Meshing Algorithms for Simulation of Hydraulically and Naturally Fractured Reservoirs with Variable Distribution of Fracture Aperture, Spacing, Length, and Strike. *SPE Reservoir Evaluation & Engineering* 18 (04): 463–80. SPE-170703-PA. https://doi.org/10.2118/170703-PA.

57. Yu, W. and Sepehrnoori, K. 2018. *Shale Gas and Tight Oil Reservoir Simulation*: Gulf Professional Publishing/Elsevier.

58. Kim, T. H. and Schechter, D. 2009. Estimation of Fracture Porosity of Naturally Fractured Reservoirs with No Matrix Porosity Using Fractal Discrete Fracture Networks. *SPE Res Eval & Eng.* **12** (2): 232–242. SPE-110720-PA. https://doi.org/10.2118/110720-PA.

59. Muralidharan, D. Chakravarthy, E. Putra, and D.S. Schechter. 2004. Investigating Fracture Aperture Distributions Under Various Stress Conditions Using X-Ray CT Scanner. Paper presented at the Canadian International Petroleum Conference, Calgary, Alberta, June. PETSOC-2004-230. https://doi.org/10.2118/2004-230.

60. Dershowitz, B., LaPointe, P., Eiben, T. et al. 2000. Integration of discrete feature network methods with conventional simulator approaches. *SPE Res Eval & Eng* **3** (02): 165–170. SPE-62498-PA. https://doi.org/10.2118/62498-PA.

61. Harstad, H., Teufel, L.W., Lorenz, J.C., 1995. Characterization and Simulation of Naturally Fractured Tight Gas Sandstone Reservoirs. Paper presented at the SPE Annual Technical Conference and Exhibition, Dallas, Texas, October. SPE-30573-MS. https://doi.org/10.2118/30573-MS.

62. Zhang, F. 2020. Numerical and Experimental Investigation of Various Surfactant and Gas Injection Techniques Improves Recovery in Unconventional Liquid Reservoirs. Dissertation. Texas A&M University, College Station, TX.

63. National Energy Technology Laboratory. NETL's Energy Data eXchange. https://edx.netl.doe.gov/group/hfts-1-phase-1-group (accessed February 2021).

64. Sun, J., Schechter, D., Lin, S. et al. 2016, August. The Impact of CT–Measured and Stress–Dependent Nonuniform Fracture Apertures on Production Performance of Microseismic–Constrained Complex Fracture Networks. Paper presented at the SPE Asia Pacific Hydraulic Fracturing Conference, Beijing, China. SPE-181783-MS. https://doi.org/10.2118/181783-MS.

65. Wood, T., Leonard, R., Senters, C. et al. 2018. Interwell Communication Study of UWC and MWC Wells in the HFTS. Paper presented at the Unconventional Resources Technology Conference, Houston, Texas, USA, 23-25 July. URTEC-2902960-MS. https://doi.org/10.15530/URTEC-2018-2902960.

66. Gale, J. F., Elliott, S. J., Li, J. Z. et al. 2019. Natural Fracture Characterization in the Wolfcamp Formation at the Hydraulic Fracture Test Site (HFTS), Midland Basin, Texas. Paper presented at the Unconventional Resources Technology Conference, Denver, Colorado, 22–24 July. URTEC-2019-644-MS. https://doi.org/10.15530/urtec-2019-644.

67. Maity, D. 2018. Microseismicity analysis for HFTS pad and correlation with completion parameters. Paper presented at the Unconventional Resources Technology Conference, Houston, Texas, USA, 23-25 July. URTEC-2902355-MS. https://doi.org/10.15530/URTEC-2018-2902355.

68. Wicker, J., Courtier, J., and Curth, P. 2016. Multivariate analytics of seismic inversion products to predict horizontal production in the Wolfcamp Formation of the Midland Basin. Paper presented at the SPE/AAPG/SEG Unconventional

Resources Technology Conference, August 1–3. URTEC-2449798-MS. https://doi.org/10.15530/URTEC-2016-2449798.

69. Kumar, A., Chao, K., Hammack, R. W. et al. 2018a. Surface Seismic Monitoring of Hydraulic Fracturing Test Site (HFTS) in the Midland Basin, Texas. Paper presented at the Unconventional Resources Technology Conference, Houston, Texas, USA, 23-25 July. URTEC-2902789-MS. https://doi.org/10.15530/URTEC-2018-2902789.

70. Kumar, A., Seth, P., Shrivastava, K. et al. 2018b. Well interference diagnosis through integrated analysis of tracer and pressure interference tests. Paper presented at the Unconventional Resources Technology Conference, Houston, Texas, USA, 23-25 July. URTEC-2901827-MS. https://doi.org/10.15530/URTEC-2018-2901827.

71. Li, T., Chu, W., and Leonard, P. A. 2019. Analysis and Interpretations of Pressure Data from the Hydraulic Fracturing Test Site (HFTS). Paper presented at the Unconventional Resources Technology Conference, Denver, Colorado, 22–24 July. URTEC-2019-233-MS. https://doi.org/10.15530/urtec-2019-233.

72. Ciezobka, J., Courtier, J., and Wicker, J. 2018. Hydraulic fracturing test site (HFTS)–project overview and summary of results. Paper presented at the Unconventional Resources Technology Conference, Houston, Texas, USA, 23-25 July. URTEC-2937168-MS. https://doi.org/10.15530/URTEC-2018-2937168.

73. Shrivastava, K., Hwang, J., and Sharma, M. 2018. Formation of Complex Fracture Networks in the Wolfcamp Shale: Calibrating Model Predictions with Core Measurements from the Hydraulic Fracturing Test Site. Paper presented at the Unconventional Resources Technology Conference, Houston, Texas, USA, 23-25 July. SPE-191630-MS. https://doi.org/10.2118/191630-MS.

74. Wicker, J., Courtier, J., Campbell, T. et al. 2018. Using Stage Level Microseismic Analysis to Correlate and Ground Truth Cored Hydraulic Fractures. Paper presented at the Unconventional Resources Technology Conference, Houston, Texas, USA, 23-25 July. URTEC-2937221-MS. https://doi.org/10.15530/URTEC-2018-2937221.

75. Trowbridge, S., Wicker, J., Courtier, J. et al. 2017. Application of microseismic to assess hydraulic fracture behavior in relation to completion design and landing zone. Paper presented at the *Unconventional Resources Technology Conference*,

Austin, Texas, 24-26 July. URTEC-2674376-MS. https://doi.org/10.15530/URTEC-2017-2674376.

76. Bazan, L. W., Larkin, S. D., Lattibeaudiere, M. G. et al. 2010. Improving production in the Eagle Ford Shale with fracture modeling, increased fracture conductivity, and optimized stage and cluster spacing along the horizontal wellbore. Paper presented at the Tight Gas Completions Conference, 2–3 November. SPE-138425-MS. https://doi.org/10.2118/138425-MS.

77. Edwards, K. L., Weissert, S., Jackson, J. B. et al. 2011. Marcellus shale hydraulic fracturing and optimal well spacing to maximize recovery and control costs. Paper presented at the SPE Hydraulic Fracturing Technology Conference, 24–26 January. SPE-140463-MS. https://doi.org/10.2118/140463-MS.

78. Stegent, N. A., and Candler, C. 2018. Downhole microseismic mapping of more than 400 fracturing stages on a multiwell pad at the Hydraulic Fracturing Test Site (HFTS): discussion of operational challenges and analytic results. Paper presented at the Unconventional Resources Technology Conference, Houston, Texas, USA, 23-25 July. URTEC-2902311-MS. https://doi.org/10.15530/URTEC-2018-2902311.

APPENDIX A

IMPACT OF FRACTAL DIMENSION FACTORS ON FRACTIRE SPATIAL DISTRIBUTION

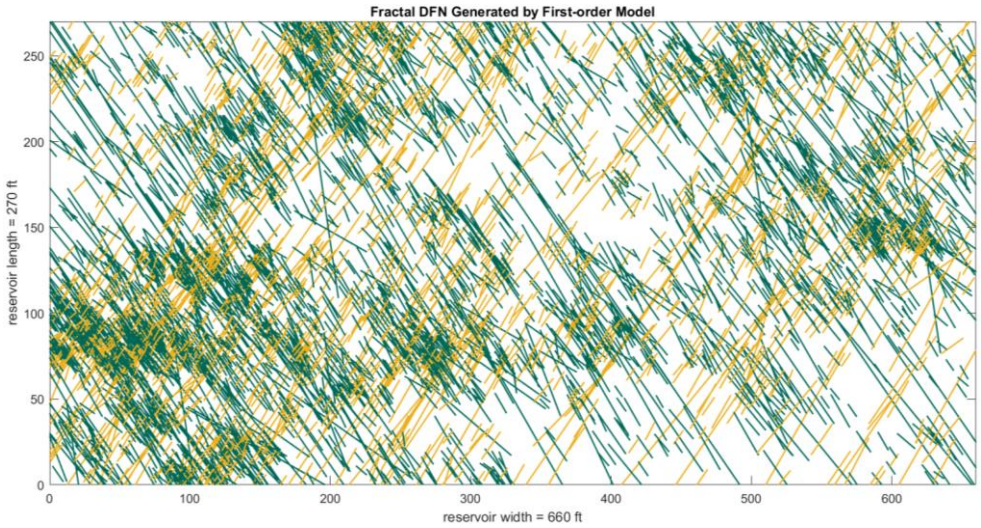

Figure A1 Stochastic fractures generated with Dc=1.5 and Dl=1.5.

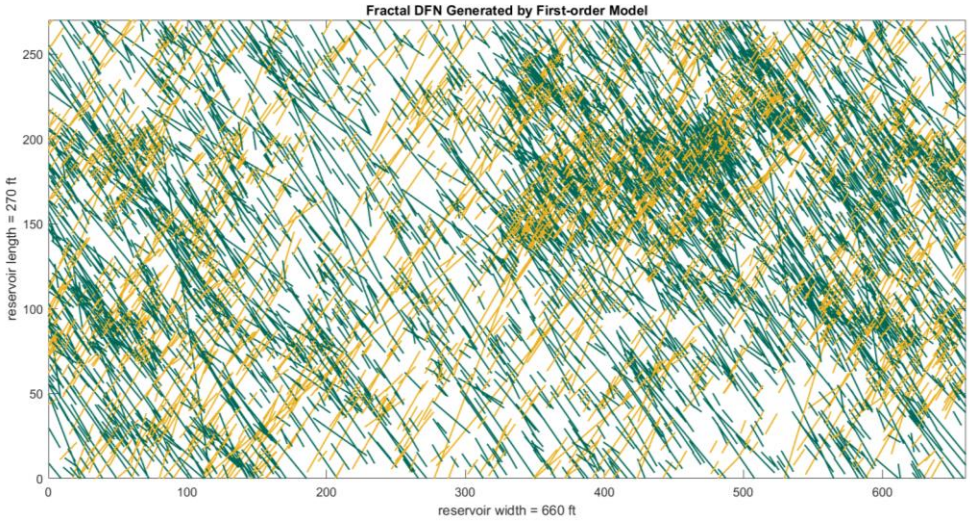

Figure A2 Stochastic fractures generated with Dc=1.75 and Dl=1.8.

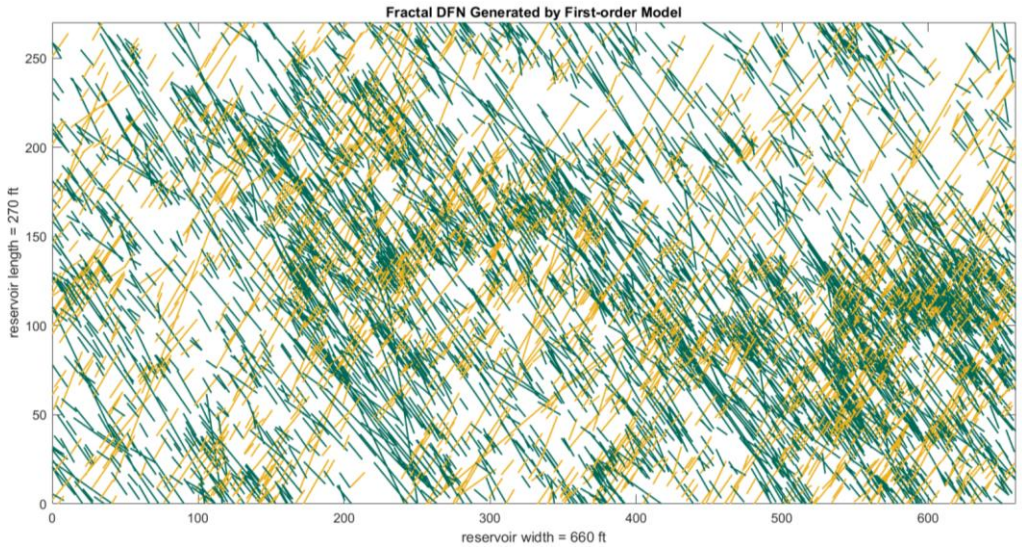

Figure A3 Stochastic fractures generated with Dc=1.75 and Dl=1.65.

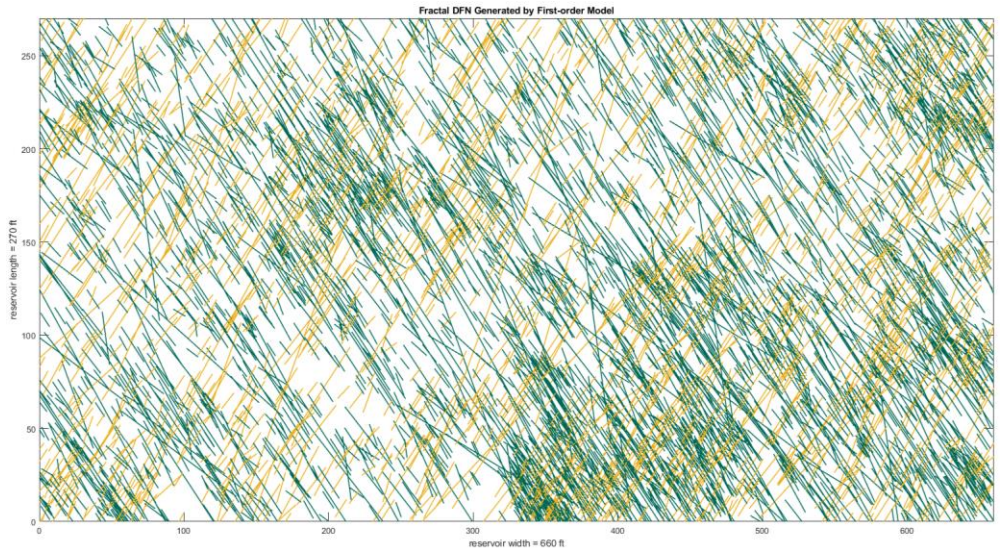

Figure A4 Stochastic fractures generated with Dc=1.85 and Dl=1.5.

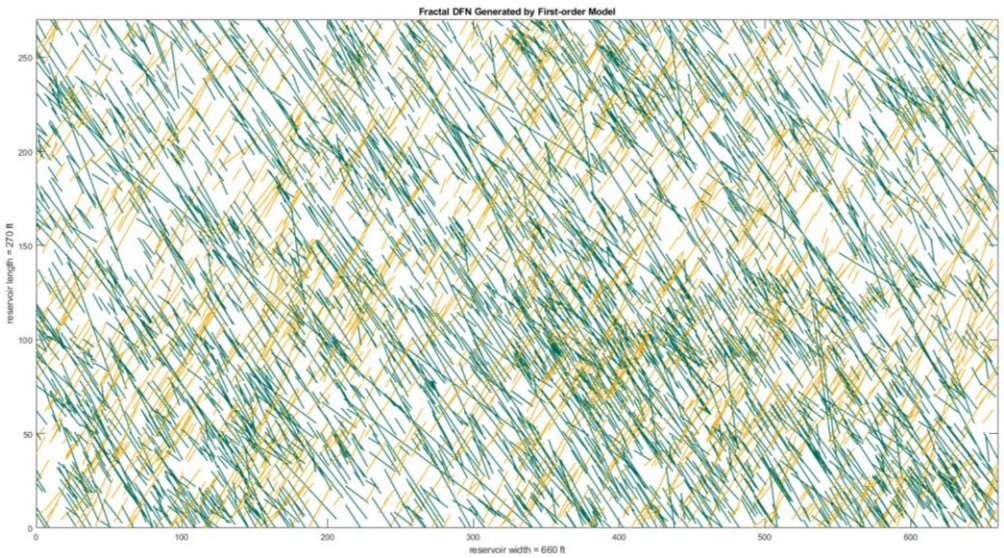

Figure A5 Stochastic fractures generated with Dc=1.85 and Dl=1.65.

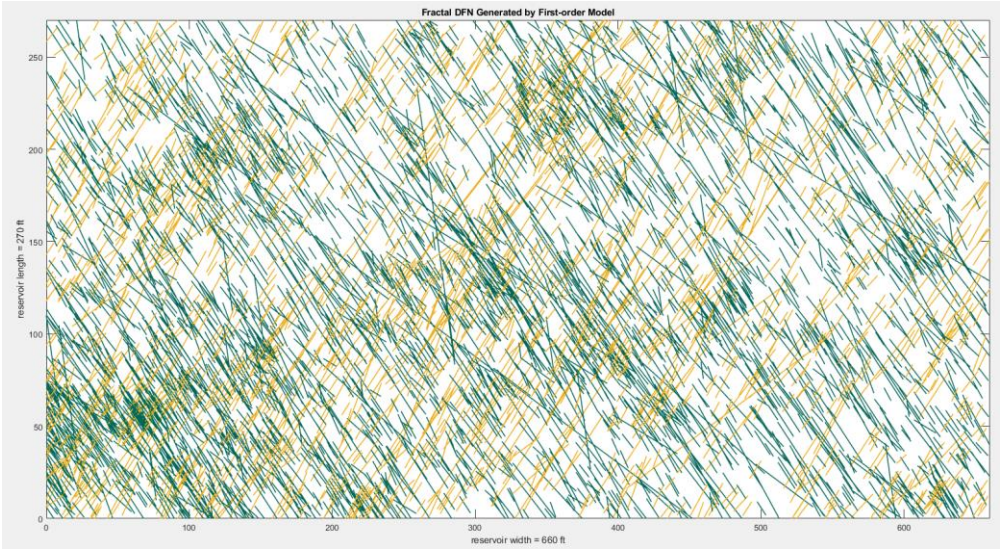

Figure A6 Stochastic fractures generated with Dc=1.85 and Dl=1.8.

From these 6 cases we can conclude that fracture clustering becomes more intense as D_c decreases. And short fractures become more abundant with increasing D_l.